

# NLO corrections to triple vector-boson production in final states with three charged leptons and two jets

---

Ansgar Denner,<sup>a</sup> Daniele Lombardi,<sup>a</sup> Santiago Lopez Portillo Chavez,<sup>a</sup> and Giovanni Pelliccioli<sup>b</sup>

<sup>a</sup>*Institut für Theoretische Physik und Astrophysik, Universität Würzburg, 97074 Würzburg, Germany*

<sup>b</sup>*Max-Planck-Institut für Physik, Boltzmannstraße 8, 85748 Garching, Germany*

*E-mail:* [ansgar.denner@uni-wuerzburg.de](mailto:ansgar.denner@uni-wuerzburg.de),

[daniele.lombardi@uni-wuerzburg.de](mailto:daniele.lombardi@uni-wuerzburg.de),

[santiago.lopez-portillo-chavez@uni-wuerzburg.de](mailto:santiago.lopez-portillo-chavez@uni-wuerzburg.de), [gpellicc@mpp.mpg.de](mailto:gpellicc@mpp.mpg.de)

**ABSTRACT:** Tri-boson production together with vector-boson scattering is a privileged channel to study the electroweak structure of the Standard Model. Upcoming LHC running stages will allow to measure these processes at unprecedented accuracy and for all possible final states, which requires to push theory predictions to still unexplored frontiers. In this work we present the first calculation for the process  $pp \rightarrow \mu^+ \mu^- e^+ \nu_e jj$  at the LHC in a tri-boson phase space. We evaluate the three LO contributions, namely the  $\mathcal{O}(\alpha^6)$ , which contains the genuine tri-boson signature, along with the  $\mathcal{O}(\alpha_s \alpha^5)$  and  $\mathcal{O}(\alpha_s^2 \alpha^4)$ , and the two  $\mathcal{O}(\alpha^7)$  and  $\mathcal{O}(\alpha_s \alpha^6)$  NLO corrections. The calculation is based on full Standard-Model matrix elements, including all resonant and non-resonant terms, complete spin correlations and interference effects. Integrated and differential cross sections are presented for a fiducial region inspired by High Luminosity LHC prospect studies. We find electroweak corrections of  $-14\%$  for the fiducial cross section, almost twice as large as for other tri-boson processes.

**KEYWORDS:** Standard Model, NLO EW, NLO QCD, off-shell, LHC, tri-boson production

---

## Contents

<b>1</b>	<b>Introduction</b>	<b>1</b>
<b>2</b>	<b>Details of the calculation</b>	<b>3</b>
2.1	Leading-order contributions	4
2.2	Next-to-leading-order corrections	9
<b>3</b>	<b>Numerical results</b>	<b>14</b>
3.1	Input parameters	14
3.2	Fiducial cross sections	16
3.3	Differential cross sections	21
<b>4</b>	<b>Conclusions</b>	<b>29</b>

---

## 1 Introduction

The successful Standard Model (SM) of particle physics is being scrutinised by the ongoing comparison of experimental measurements from the Large Hadron Collider (LHC) and theoretical predictions. Any statistically significant discrepancy between theory and experiments can point to a still poor understanding of nature and open the path to new physics discoveries. By now, the huge amount of data that has been collected at the LHC continually confirmed any SM-based prediction, at least within the level of accuracy that both the experimental and the theory community can provide so far. However, large improvements are expected from the upcoming full Run-3 dataset and even more from the future high-luminosity (HL) stage of the LHC, where statistical uncertainties in the experimental measurements will be considerably reduced, and which might shed light on still unexplored or poorly known sectors of the SM. Among these, some parts of the electroweak (EW) sector, which is a fundamental building block of the SM, are still surprisingly loosely constrained owing to the complexity of the measurements of processes which are sensitive to it. Among these rare processes, vector-boson scattering (VBS) and triple vector-boson production are the most prominent ones to directly access triple and quartic gauge couplings and to study the mechanism of EW symmetry breaking. Since all of these production mechanisms have already been investigated by experimental collaborations at the LHC and will be known with a much higher precision in the next years, a solid control on the theory predictions requires to compute these processes at the best-possible accuracy in all of their final states.

Despite the intrinsic complexity, VBS measurements have already received remarkable attention at the LHC in the last years especially in the fully-leptonic final state, together with some more recent searches in the semi-leptonic final state (see for instance Refs. [1, 2])

for a general overview on the status of VBS studies). On the other hand, the production of three gauge bosons is a much less explored signal, since its very low cross section and the overwhelming background render its measurement highly elusive. If one excludes tri-boson measurements involving at least one photon [3–8], only a few searches for triple massive-gauge-boson production have been performed so far, specifically for  $W^\pm W^\pm W^\mp$  at 8 TeV [9] and 13 TeV [10] by ATLAS and CMS, respectively, followed by evidence for massive tri-boson production in Ref. [11] and finally its observation by the two collaborations in Refs. [12, 13], where all possible massive-boson combinations have been considered. Owing to the undoubted relevance of this process for complementing our knowledge of the SM, new measurements are expected to be carried out to constrain the tri-boson signal further, as confirmed by an ATLAS prospect study for the HL phase of the LHC in Ref. [14].

This scenario poses new challenges for the theory community. Indeed, keeping up with the progress achieved on the experimental side requires to improve the accuracy at which VBS and tri-boson processes are known but also to test existing ones for fiducial phase-space regions which have not been considered yet. This is the case for the tri-boson phase space, which has by now received very little attention owing to its hitherto marginal role in experimental searches. Computations for tri-boson production mostly exist as part of full VBS ones, to which they contribute as a background. For the latter processes many results are available in the literature, with state-of-the-art calculations for the fully leptonic final states including next-to-leading order (NLO) QCD and NLO EW corrections [15–18], or even the complete NLO corrections to  $W^+W^+$  [19] and  $ZZ$  [20] scattering. Additionally, NLO EW corrections have been matched to a QED shower and interfaced to a QCD shower for  $W^+W^+$  scattering in Ref. [21]. Even if to a lesser extent, some VBS calculations in the semi-leptonic final state are also becoming available, by now only at leading order (LO) [22, 23]. This rich and potentially increasing list of results for VBS should be compared to the much lower number of studies focusing on triple massive-gauge-boson production. In fact, while tri-boson calculations exist at NLO QCD [24, 25] and NLO QCD+EW [26, 27] accuracy for stable vector bosons or with LO decays in the narrow-width approximation [28, 29] since many years, the off-shell description of such processes has been limited to NLO QCD accuracy in the fully leptonic channel for a long time [30, 31], and NLO EW corrections were only achieved a few years ago [32, 33]. The case of tri-boson production with one vector boson decaying hadronically has been addressed only very recently in Ref. [34], where the full set of NLO corrections for tri-boson and WH production in the  $W^+W^+jj$  channel have been considered. In the same work the NLO QCD contribution has been matched to the Sherpa parton shower [35] for the QCD and EW production modes, where for the latter EW corrections have been included via the  $EW_{\text{virt}}$  approximation [36, 37]. The importance of tri-boson processes as probes of possible new-physics effects beyond the SM is witnessed by very recent LO [38] and NLO QCD [39] studies in the framework of the SM effective field theory.

The production mechanism of three massive vector bosons in a non-fully-leptonic final state has a clear overlap with VBS from a theoretical point of view. Indeed, fully off-shell theory calculations are only sensitive to the final state of the process, while they account for all possible intermediate resonances. The two production modes are actually defined

and distinguished by the fiducial phase-space that is used to enhance a specific signal over a certain background. As shown in Ref. [34] in the context of tri-boson and VBS production, a change in the definition of the fiducial volume can lead to phenomenologically interesting outcomes, for instance a different behaviour of the EW corrections. That already represents a strong enough theoretical motivation to study tri-boson production for this yet little explored semi-leptonic final state. Moreover, the latter, which has a larger cross section compared to its fully-leptonic counterpart, is expected to become accessible at the LHC and by that time it will definitely play a relevant role in increasing our understanding of the process.

In this work we provide one more calculation for tri-boson production with one hadronically decaying vector boson, specifically in the  $W^+Zjj$  channel. This channel has been studied before in the VBS phase space in Ref. [16]. In the present work, all LO contributions to the process have been computed, namely  $\mathcal{O}(\alpha^6)$ ,  $\mathcal{O}(\alpha_s\alpha^5)$ , and  $\mathcal{O}(\alpha_s^2\alpha^4)$ . Moreover, the  $\mathcal{O}(\alpha^7)$  and  $\mathcal{O}(\alpha_s\alpha^6)$  corrections have also been obtained exactly. A detailed description of the calculation for the different perturbative contributions is presented in Section 2. Then we report numerical results in Section 3, obtained in a phase space devised to enhance the tri-boson signal and inspired by the HL LHC prospect studies from ATLAS [14]. After fixing our setup in Section 3.1, both inclusive and differential cross sections are reported in Sections 3.2 and 3.3, respectively. We conclude by commenting on the main outcomes of our study in Section 4.

## 2 Details of the calculation

In this paper we investigate the process

$$pp \rightarrow \mu^+\mu^-e^+\nu_e jj \quad (2.1)$$

at the LHC in a phase space that is devised to enhance the tri-boson production mechanism.

We evaluate the process for the full set of LO contributions, namely  $\mathcal{O}(\alpha^6)$ ,  $\mathcal{O}(\alpha_s\alpha^5)$ , and  $\mathcal{O}(\alpha_s^2\alpha^4)$ . Only the  $\mathcal{O}(\alpha^6)$  includes the tri-boson signal, whereas the remaining two orders exclusively describe its irreducible background. We additionally compute the two NLO corrections to the  $\mathcal{O}(\alpha^6)$ , which contribute at  $\mathcal{O}(\alpha^7)$  and  $\mathcal{O}(\alpha_s\alpha^6)$ . For the latter order, EW corrections to  $\mathcal{O}(\alpha_s\alpha^5)$  are also properly included, since they can not be disentangled from the QCD corrections to  $\mathcal{O}(\alpha^6)$  (see Section 2.2.2). That is illustrated in Fig. 1, where we show a summary of all perturbative orders which are relevant for the process in Eq. (2.1) up to NLO. Among these, we refrain from evaluating the  $\mathcal{O}(\alpha_s^2\alpha^5)$  and  $\mathcal{O}(\alpha_s^3\alpha^4)$ , since they only comprise corrections to the tri-boson background.

The calculation has been performed with the in-house program MOCANLO, a multi-channel Monte Carlo generator that has already proven suitable for the evaluation of processes with high-multiplicity final states and an intricate resonance structure, like the one presented in this article. It is interfaced with RECOLA [40, 41], which provides the tree-level SM matrix elements together with the spin-correlated and colour-correlated ones, needed for the definition of the unintegrated subtraction counterterms. RECOLA computes all the

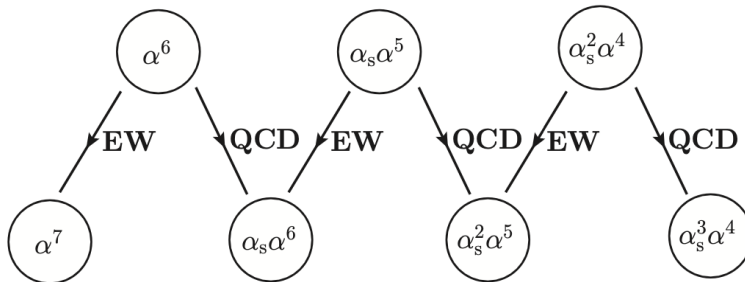


**Figure 1.** Perturbative contributions to the process  $pp \rightarrow \mu^+ \mu^- e^+ \nu_e jj$ .

required one-loop amplitudes using the COLLIER library [42] to perform the reduction and numerical evaluation of one-loop integrals [43–45].

We work in a five-flavour scheme and assume a diagonal quark-mixing matrix with unit entries throughout our calculations. We explicitly consider a final state involving two different lepton generations. Predictions with two same-sign same-flavour leptons can be roughly recovered by multiplying our results by appropriate factors that account for the number of identical particles in the final state. Interference effects, which are neglected by this procedure, are expected to be small as was verified for fully-leptonic tri-boson processes in Refs. [32, 33].

Even though the phase space defined in Section 3 is devised to increase the tri-boson signal, our calculation consistently includes all possible resonant and non-resonant topologies and exactly retains interference effects. Owing to our choice of flavour scheme, the cross section for the process in Eq. (2.1) also receives contributions from partonic processes with bottom quarks both as initial and as final states. In the latter case the bottom quarks can give rise to a top-quark resonance, which contaminates our genuine tri-boson signal in a non-negligible way. As discussed in the following, we performed a complete LO calculation for these contributions but do not include them in our final predictions nor evaluate them at NLO. Indeed, they should rather be considered as part of a different LHC process, and we drop them by assuming a perfect b-jet tagging and veto.

Since experimental analyses often separate photon-production from jet-production processes, we do not treat final-state photons as jets. This experimentally-motivated choice has important consequences in the treatment of NLO corrections at  $\mathcal{O}(\alpha_s \alpha^6)$ , where different subtleties arise, as discussed in Section 2.2.2.

## 2.1 Leading-order contributions

Using  $g$  and  $g_s$  to denote the EW and strong coupling constants, respectively, the amplitude for the process in Eq. (2.1) receives contributions at  $\mathcal{O}(g^6)$ ,  $\mathcal{O}(g_s g^5)$ , and  $\mathcal{O}(g_s^2 g^4)$ . At the squared-amplitude level three different LO contributions are present, namely  $\mathcal{O}(\alpha^6)$ ,  $\mathcal{O}(\alpha_s \alpha^5)$ , and  $\mathcal{O}(\alpha_s^2 \alpha^4)$ .

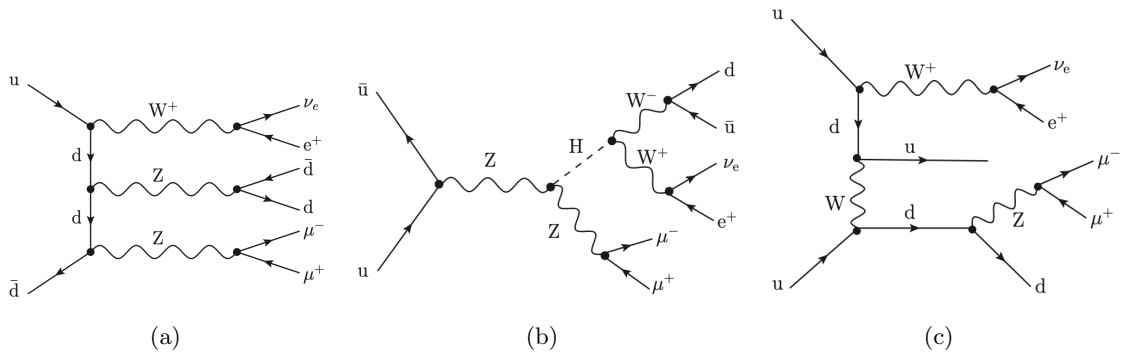


**Figure 2.** Sample  $\mathcal{O}(g^6)$  diagrams for quark-induced channels. Shown are topologies compatible with a tri-boson signature [2(a)], Higgs strahlung [2(b)], and a doubly-resonant contribution to the tri-boson background [2(c)].

### 2.1.1 Contributions to $\mathcal{O}(\alpha^6)$

The  $\mathcal{O}(\alpha^6)$  is the one containing our signal, comprising two leptonically-decaying gauge bosons and a hadronically-decaying one, which can either be a Z or a W boson. For the specific choice of leptonic final states in Eq. (2.1), charge conservation forces the hadronically-decaying W boson to be negatively charged.

The bulk of the cross section arises from partonic channels that are compatible with a tri-boson signal, namely

$$q_1 \bar{q}_2 \rightarrow \mu^+ \mu^- e^+ \nu_e q_3 \bar{q}_4, \quad q_i \in S_q = \{u, d, s, c\}, \quad (2.2)$$

where  $q_3$  and  $\bar{q}_4$  belong to the same quark generation and whose electric charge  $Q$  is such that  $Q(q_3) + Q(\bar{q}_4) \in \{-1, 0\}$ . Predictions for these channels are dominated by genuine tri-boson topologies [Fig. 2(a)] or Higgs-strahlung diagrams [Fig. 2(b)]. All remaining quark-induced channels involving quarks  $q_i \in S_q$  are not compatible with tri-boson production and can be summarised in the reactions

$$q_1 q_2 \rightarrow \mu^+ \mu^- e^+ \nu_e q_3 q_4, \quad \bar{q}_1 \bar{q}_2 \rightarrow \mu^+ \mu^- e^+ \nu_e \bar{q}_3 \bar{q}_4, \quad q_1 \bar{q}'_2 \rightarrow \mu^+ \mu^- e^+ \nu_e q_3 \bar{q}'_4, \quad (2.3)$$

where the notation  $\bar{q}'_i$  highlights that  $q_1$  and  $\bar{q}'_2$  as well as  $q_3$  and  $\bar{q}'_4$  belong to different generations. These channels can be at most doubly resonant and therefore represent a background to the tri-boson signature. Indeed they can include for instance VBS-like topologies or  $t$ -channel configurations, as the one illustrated in Fig. 2(c), where the two quark lines running from the initial to the final state exchange a  $t$ -channel vector boson. However, at the perturbative order we are considering, they are largely suppressed by the selection cuts defining the signal region, in particular the cut  $M_{j_1 j_2} < 100$  GeV in Eq. (3.6).

At  $\mathcal{O}(\alpha^6)$ , two additional kinds of partonic channels are included as part of our signal, namely the  $\gamma\gamma$ - and  $b\bar{b}$ -induced ones:

$$\gamma\gamma \rightarrow \mu^+ \mu^- e^+ \nu_e q_1 \bar{q}_2, \quad b\bar{b} \rightarrow \mu^+ \mu^- e^+ \nu_e q_1 \bar{q}_2. \quad (2.4)$$

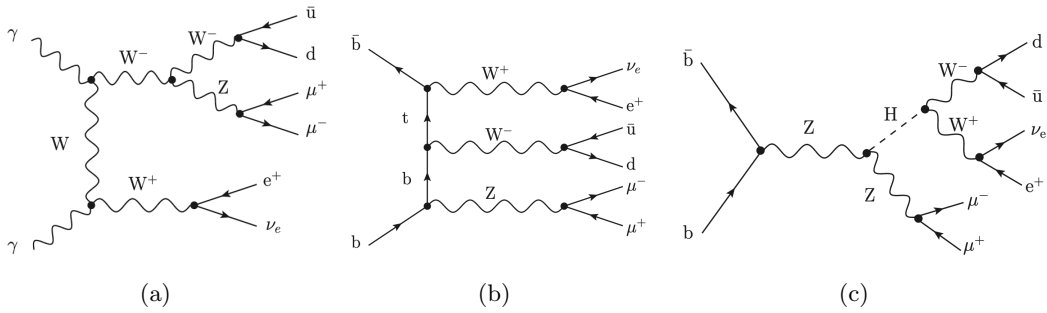


**Figure 3.** Sample  $\mathcal{O}(g^6)$  diagrams for  $\gamma\gamma$ - and  $b\bar{b}$ -induced channels. Shown are topologies compatible with a tri-boson signature for the  $\gamma\gamma$  channel [3(a)] and the  $b\bar{b}$  channel [3(b)]. For the  $b\bar{b}$  case a Higgs-strahlung contribution is also shown [3(c)].

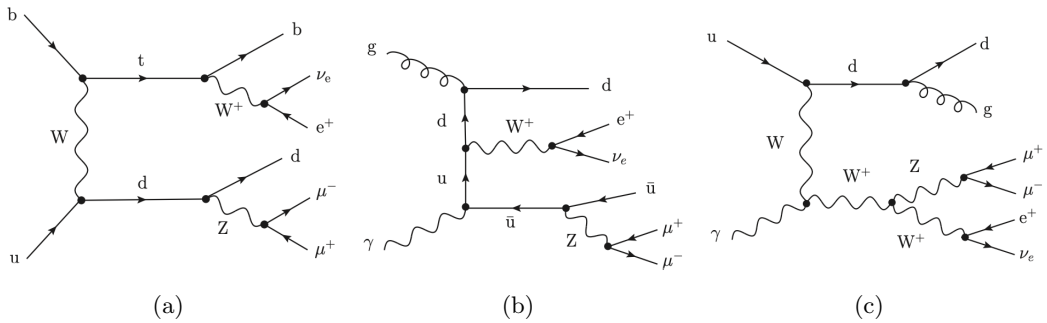


**Figure 4.** Sample  $\mathcal{O}(g^6)$  diagram for the  $q b$ -induced channel with an  $s$ -channel top-quark resonance [4(a)] and sample  $\mathcal{O}(g_s g^5)$  diagrams for the  $g\gamma$ - and  $\gamma q$ -induced contributions [4(b) and 4(c)].

Indeed, both of them contribute to tri-boson production with triply-resonant diagrams like the ones shown in Fig. 3, which partly compensate for the suppression from photon- and bottom PDFs. In particular, we note that the cross section for  $b\bar{b}$ -initiated channels is dominated by topologies involving a non-resonant  $t$ -channel top quark [Fig. 3(b)] and Higgs-strahlung diagrams [Fig. 3(c)].

To assess the impact of additional background sources to our signal region, we also evaluate partonic processes involving bottom quarks in the final states, which we separate and ultimately exclude in our final predictions with the assumption of a perfect  $b$ -jet veto.<sup>1</sup> They belong to the following two classes:

$$\begin{aligned}
q_1 b &\rightarrow \mu^+ \mu^- e^+ \nu_e q_2 b, & q_1 \bar{b} &\rightarrow \mu^+ \mu^- e^+ \nu_e q_2 \bar{b}, \\
\bar{q}_1 b &\rightarrow \mu^+ \mu^- e^+ \nu_e \bar{q}_2 b, & \bar{q}_1 \bar{b} &\rightarrow \mu^+ \mu^- e^+ \nu_e \bar{q}_2 \bar{b}, \\
q_1 \bar{q}_2 &\rightarrow \mu^+ \mu^- e^+ \nu_e b \bar{b}.
\end{aligned} \tag{2.5}$$

The contributions in Eq. (2.5) with a single  $b$  or  $\bar{b}$  quark in the initial state can be at most doubly resonant in the vector bosons but are enhanced by the appearance of a top-quark resonance, as in the diagram shown in Fig. 4(a). For the contributions in Eq. (2.5) with a

<sup>1</sup>These processes contribute to  $tZj$  production, which has been investigated in Ref. [46].

final-state  $b\bar{b}$  pair, top-quark-resonant topologies are accompanied by tri-boson diagrams, where the bottom quarks result from the hadronic decay of a Z boson.

### 2.1.2 Contributions to $\mathcal{O}(\alpha_s\alpha^5)$

The  $\mathcal{O}(\alpha_s\alpha^5)$  can only receive contributions from topologies which are at most doubly resonant in the vector bosons and therefore part of the tri-boson background. Two different combinations of amplitudes enter this perturbative order: interferences of  $\mathcal{O}(g^6)$  and  $\mathcal{O}(g_s^2g^4)$  amplitudes and squares of  $\mathcal{O}(g_s g^5)$  amplitudes.

Contributions involving two initial-state quarks can only appear as interference terms. The latter vanish owing to colour algebra, except for the case where  $t$ -channel diagrams interfere with  $u$ - and/or  $s$ -channel ones. This explains why no contribution involving bottom quarks, either as initial or final states, appears at this order.

At  $\mathcal{O}(g_s g^5)$  only amplitudes with one external gluon and one external photon are possible. That allows for new partonic channels, i.e. the  $g\gamma$ -,  $\gamma q$ -, and  $\gamma\bar{q}$ -induced ones:

$$g\gamma \rightarrow \mu^+\mu^-e^+\nu_e q_1 \bar{q}_2, \quad \gamma q_1 \rightarrow \mu^+\mu^-e^+\nu_e q_2 g, \quad \gamma \bar{q}_1 \rightarrow \mu^+\mu^-e^+\nu_e \bar{q}_2 g. \quad (2.6)$$

No  $\gamma b$ - or  $\gamma\bar{b}$ -induced channels contribute to our results. The former channel is simply forbidden by charge conservation. The second one can just be constructed by including a top quark in the final state at this perturbative order. However, since the top quark is treated as a resonance throughout our calculation, it can not be part of the final state, so that all  $\gamma\bar{b}$ -induced diagrams are discarded. Some illustrative diagrams for the  $g\gamma$  and  $\gamma q$  partonic processes are reported in Figs. 4(b) and 4(c), respectively. It is worth noting that the bulk of the  $\gamma q/\gamma\bar{q}$  cross section originates from diagrams involving a  $q \rightarrow gq$  or  $\bar{q} \rightarrow g\bar{q}$  final-state splitting as in Fig. 4(c). Indeed, this final-state quark–gluon pair can easily be misidentified as a pair of jets from a would-be hadronically-decaying vector boson, so that the event can pass the tri-boson selection cuts. That is in contrast to what happens for the  $g\gamma$  channel, where the two final-state quarks are connected by a  $t$ -channel fermion line and on average have a larger invariant mass, which renders it less likely for the events to pass the cuts. This fact is important to understand the relative size of these contributions observed in Section 3.2.

### 2.1.3 Contributions to $\mathcal{O}(\alpha_s^2\alpha^4)$

At this perturbative order only squares of  $\mathcal{O}(g_s^2g^4)$  amplitudes contribute, which are again at most doubly resonant and comprise either an internal gluon propagator or two external gluon lines.

Among contributions with no external gluons, the dominant ones involve  $q\bar{q}'$ -,  $qq'$ -, and  $\bar{q}\bar{q}'$ -induced channels. These can only proceed via the exchange of an internal  $t$ -channel gluon, as exemplified in Fig. 5(a), while the  $b\bar{b}$ -induced ones, which are largely suppressed by the bottom PDFs, only include diagrams with an  $s$ -channel gluon, as shown in Fig. 5(b). As for  $\mathcal{O}(\alpha^6)$ , a sizeable fraction of the cross section arises from channels with final-state bottom quarks [Fig. 5(c)], which at this order are not enhanced by the presence of a top-quark resonance.



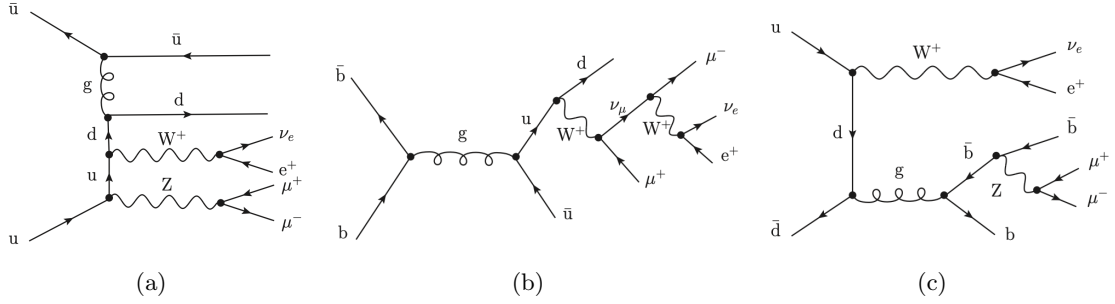


**Figure 5.** Sample  $\mathcal{O}(g_s^2 g^4)$  diagrams for light-quark-induced channels [5(a)], bottom-induced channels [5(b)] and for channels with two bottom quarks in the final state [5(c)].

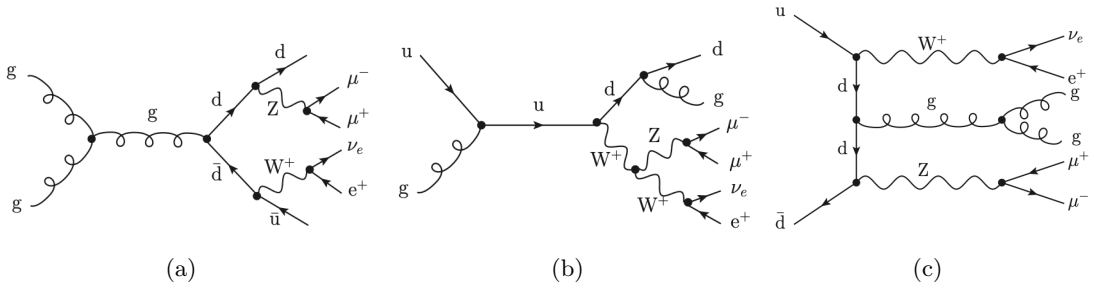


**Figure 6.** Sample  $\mathcal{O}(g_s^2 g^4)$  diagrams involving two external gluons. Shown are topologies with two initial-state gluons [6(a)], one initial-state gluon [6(b)], and two final-state gluons [6(c)].

Channels including external gluons provide by far the dominant contributions across all perturbative orders considered in this paper and are described by the reactions

$$\begin{aligned}
 gg &\rightarrow \mu^+ \mu^- e^+ \nu_e q_1 \bar{q}_2, & q_1 \bar{q}_2 &\rightarrow \mu^+ \mu^- e^+ \nu_e gg, \\
 q_1 g &\rightarrow \mu^+ \mu^- e^+ \nu_e q_2 g, & \bar{q}_1 g &\rightarrow \mu^+ \mu^- e^+ \nu_e \bar{q}_2 g.
 \end{aligned}
 \tag{2.7}$$

Although  $gg$ -induced channels are expected to be enhanced by the gluon PDFs, they appear to be suppressed by the definition of the tri-boson fiducial region, where the final-state QCD partons are required to have an invariant mass compatible with a hadronically-decaying vector boson [see Fig. 6(a)]. Indeed, the invariant mass of the two final-state quarks connected by internal fermion lines is expected to have higher values on average. This is not the case for the  $qg/\bar{q}g$ -induced channels or the  $q\bar{q}$  ones with two final-state gluons, shown in Fig. 6(b) and Fig. 6(c), respectively. In each case, the  $qg$  and  $g\bar{q}$  pair arising from a QCD-singular splitting can have an invariant mass of the order of  $M_W$  and therefore can be reconstructed as a vector boson.

Note that channels involving bottom quarks can not be obtained from Eq. (2.7) with the replacement  $(q_1, \bar{q}_2) \rightarrow (b, \bar{b})$  or  $(q_1, q_2) \rightarrow (b, b)$ , since charge conservation forces  $Q(q_1) + Q(\bar{q}_2) = Q(q_1) - Q(q_2) = +1$ .

## 2.2 Next-to-leading-order corrections

In our calculation, we consider the NLO EW and QCD corrections to the  $\mathcal{O}(\alpha^6)$  cross section, which accounts for the signal. We also evaluate NLO EW corrections to  $\mathcal{O}(\alpha_s\alpha^5)$ , since they can not be disentangled from NLO QCD corrections to  $\mathcal{O}(\alpha^6)$  in an infrared(IR)-safe manner. Nevertheless, NLO corrections of orders 2 and more in  $\alpha_s$  are not computed, i.e. we do consider neither NLO QCD corrections to the  $\mathcal{O}(\alpha_s\alpha^5)$  cross section nor NLO QCD and EW corrections to the  $\mathcal{O}(\alpha_s^2\alpha^4)$  cross section. The latter two would represent corrections to the background and can safely be dropped without breaking gauge invariance or spoiling the IR safety of our calculation.

Both QCD and QED singularities of soft and collinear origin that plague the real contributions are treated using the dipole subtraction formalism [47–50]. The initial-state collinear singularities are absorbed in the PDFs in the  $\overline{\text{MS}}$  factorisation scheme.

Throughout our calculation, the complex-mass scheme for all unstable particles is used [51–54] resulting in complex input values for the EW boson masses, the top-quark mass, and the EW mixing angle,

$$\mu_B^2 = M_B^2 - i\Gamma_B M_B \quad (B \in W, Z, H), \quad \mu_t^2 = m_t^2 - i\Gamma_t m_t, \quad \cos^2 \theta_w = \frac{\mu_W^2}{\mu_Z^2}. \quad (2.8)$$

### 2.2.1 Contributions to $\mathcal{O}(\alpha^7)$

NLO EW corrections to the  $\mathcal{O}(\alpha^6)$  comprise two kinds of contributions. The first class is represented by single-photon-induced terms, which are purely real corrections to EW-mediated quark-induced channels and described by the reactions

$$\gamma q_1 \rightarrow \mu^+ \mu^- e^+ \nu_e q_2 q_3 \bar{q}_4, \quad \gamma \bar{q}_1 \rightarrow \mu^+ \mu^- e^+ \nu_e \bar{q}_2 q_3 \bar{q}_4. \quad (2.9)$$

The presence of a photon in the initial state only introduces an initial-state singularity, which is absorbed via PDF renormalisation. A representative diagram for this class is shown in Fig. 7(a).

The second class of NLO EW contributions includes both virtual and real corrections to the partonic channels entering at  $\mathcal{O}(\alpha^6)$ . The real corrections to the  $\gamma\gamma$  channel, namely

$$\gamma\gamma \rightarrow \mu^+ \mu^- e^+ \nu_e q_1 \bar{q}_2 \gamma, \quad (2.10)$$

have a larger number of singular regions compared to the case in Eq. (2.9), since the real final-state photon can be radiated both by final-state quarks and by charged leptons, as illustrated in Figs. 7(b) and 7(c), respectively. However, the real channels with two quarks in the initial state,

$$\begin{aligned} q_1 \bar{q}_2 &\rightarrow \mu^+ \mu^- e^+ \nu_e q_3 \bar{q}_4 \gamma, & q_1 q_2 &\rightarrow \mu^+ \mu^- e^+ \nu_e q_3 q_4 \gamma, & \bar{q}_1 \bar{q}_2 &\rightarrow \mu^+ \mu^- e^+ \nu_e \bar{q}_3 \bar{q}_4 \gamma, \\ q_1 \bar{q}'_2 &\rightarrow \mu^+ \mu^- e^+ \nu_e q_3 \bar{q}'_4 \gamma, & b_1 \bar{b}_2 &\rightarrow \mu^+ \mu^- e^+ \nu_e q_1 \bar{q}_2 \gamma, \end{aligned} \quad (2.11)$$

are the ones with the richest IR structure, since they can contain both initial- and final-state collinear singularities (see Figs. 7(d) and 7(e) for exemplary diagrams). For this

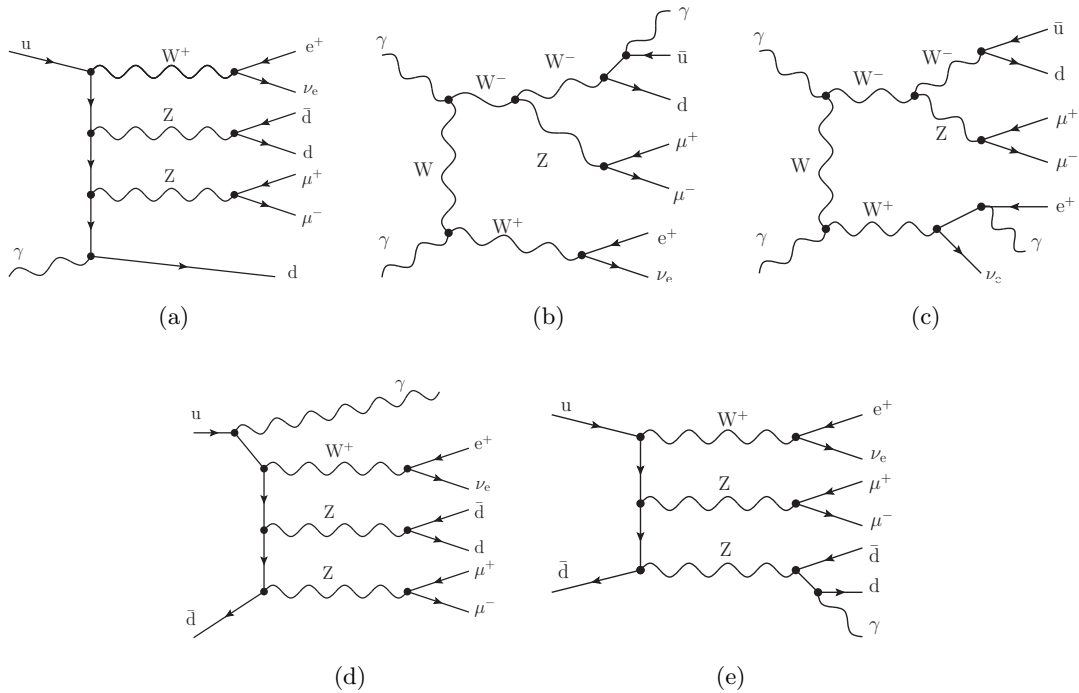


**Figure 7.** Sample  $\mathcal{O}(g^7)$  diagrams involving external photons. We show topologies with one and two initial-state photons [7(a), 7(b), and Fig. 7(c)] as well as with initial-state quark–antiquark pairs [7(d) and 7(e)].

reason, the subtraction procedure and the numerical integration of these terms are among the most computationally intensive in our calculation.

For this second class of partonic processes the evaluation of the virtual contributions, whose amplitudes result from the interference of  $\mathcal{O}(g^6)$  diagrams with  $\mathcal{O}(g^8)$  loop ones, is also a computationally expensive part of the calculation. The complexity arises both from the number of loop diagrams to be accounted for, which can become significantly large for fully EW diagrams, and from the evaluation of the loop integrals, which can involve up to 8-point functions with tensor rank 4 [Fig. 8(a)] and 5 [Fig. 8(b)] for the quark- and  $\gamma\gamma$ -induced channels, respectively.

### 2.2.2 Contributions to $\mathcal{O}(\alpha_s\alpha^6)$

This perturbative order receives contributions both from NLO QCD corrections to  $\mathcal{O}(\alpha^6)$  and from NLO EW corrections to  $\mathcal{O}(\alpha_s\alpha^5)$ .

As far as the real contributions are concerned, one can still distinguish the two kinds of corrections. We start considering real QCD corrections to  $\mathcal{O}(\alpha^6)$ , which result from squaring amplitudes of  $\mathcal{O}(g_s g^6)$ . These comprise partonic channels at  $\mathcal{O}(\alpha^6)$  with an additional

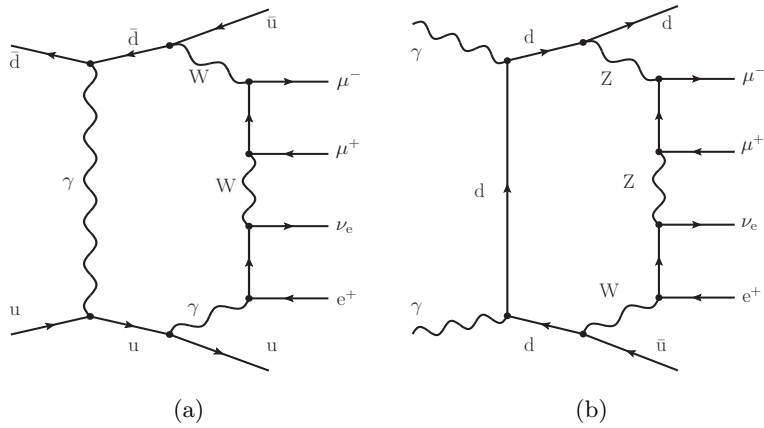


**Figure 8.** One-loop diagrams of  $\mathcal{O}(g^8)$  involving tensor integrals of rank 4 [8(a)] and rank 5 [8(b)].

final-state gluon,

$$q_1 \bar{q}_2 \rightarrow \mu^+ \mu^- e^+ \nu_e q_3 \bar{q}_4 g, \quad (2.12)$$

$$q_1 q_2 \rightarrow \mu^+ \mu^- e^+ \nu_e q_3 q_4 g, \quad \bar{q}_1 \bar{q}_2 \rightarrow \mu^+ \mu^- e^+ \nu_e \bar{q}_3 \bar{q}_4 g, \quad q_1 \bar{q}'_2 \rightarrow \mu^+ \mu^- e^+ \nu_e q_3 \bar{q}'_4 g, \quad (2.13)$$

$$\gamma \gamma \rightarrow \mu^+ \mu^- e^+ \nu_e q_1 \bar{q}_2 g, \quad b \bar{b} \rightarrow \mu^+ \mu^- e^+ \nu_e q_1 \bar{q}_2 g, \quad (2.14)$$

as well as new partonic channels involving an initial-state gluon,

$$q_1 g \rightarrow \mu^+ \mu^- e^+ \nu_e q_2 q_3 \bar{q}_4, \quad \bar{q}_1 g \rightarrow \mu^+ \mu^- e^+ \nu_e \bar{q}_2 q_3 \bar{q}_4. \quad (2.15)$$

We note that, although the terms in Eqs. (2.12)–(2.15) represent NLO QCD corrections, in general both QCD and QED Catani–Seymour (CS) dipoles are needed to properly account for all IR singularities. This is indeed true for all channels with at least one initial-state quark, while the  $\gamma\gamma$ - and  $b\bar{b}$ -induced channels in Eq. (2.14) have a simpler structure and only suffer from QCD divergences. In Fig. 9(a) a diagram with an initial-state collinear QED singularity from a  $q \rightarrow q\gamma$  splitting is shown as an example. Final-state collinear QED divergences can also appear and are separately discussed in the following.

Among the real channels with at least one initial-state quark  $q$ , the ones in Eq. (2.13), which are not compatible with a tri-boson signal, have the simpler IR structure, since QED CS dipoles are required only for initial-state singularities besides the QCD dipoles. However, the behaviour of the NLO corrections is particularly interesting for these partonic processes. Indeed, despite the high suppression of the  $\mathcal{O}(\alpha^6)$  induced by the selection cuts, they receive large and positive corrections at  $\mathcal{O}(\alpha_s \alpha^6)$ , as it is confirmed by the results in Section 3.2. This can be understood as follows: While all contributions with a Born-like kinematics are largely cut away from our signal region by the cuts in Eqs. (3.5) and (3.6), this is not the case for the real contributions, where the additional gluon radiation allows to elude the di-jet invariant-mass cut of Eq. (3.6) whenever a quark–gluon pair is misidentified as the hadronic decay of a would-be vector boson. These contributions obviously miss the enhancement of one vector-boson resonance. On the other hand, they involve a  $t$ -channel

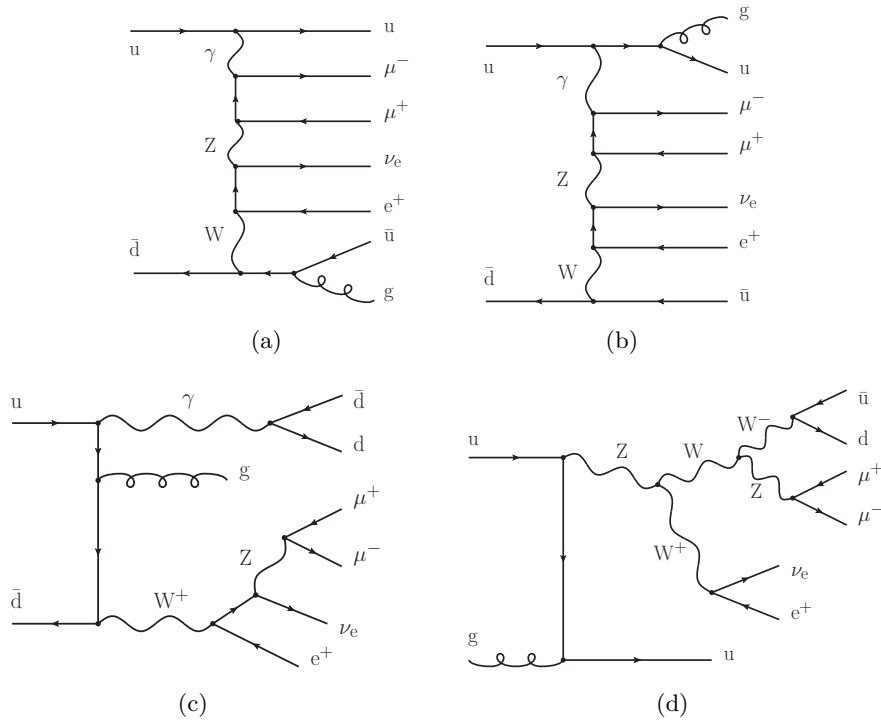


**Figure 9.** Exemplary diagrams of  $\mathcal{O}(g_s g^6)$  with one external gluon involving an initial-state singularity from a  $q \rightarrow q\gamma$  splitting [9(a)], a final-state singularity from a  $\gamma \rightarrow q\bar{q}$  splitting [9(c)] and without QED singularities [9(b) and 9(d)].

vector boson coupled to an incoming and outgoing quark as in Fig. 9(b), which is enhanced at high energies similar to VBS topologies [34].

The remaining channels with at least an initial-state quark  $q$  are the tri-boson-compatible quark-induced ones in Eq. (2.12) and the quark–gluon-initiated ones in Eq. (2.15), for which diagrams are shown in Figs. 9(a)–9(c) and Fig. 9(d), respectively. Both of them admit a virtual photon with a subsequent splitting into a  $q\bar{q}$  pair in the final state, i.e. via  $\gamma^* \rightarrow q\bar{q}$  [see Fig. 9(c)], which renders the treatment of IR QED singularities more involved. In the limit of vanishing virtuality of the photon the real amplitude develops a collinear singularity. The collinear quark pair is clustered into a single jet and the singular event mapped into a Born-like topology. By virtue of the KLN theorem [55, 56], this singularity would be cancelled by a proper inclusion of virtual EW corrections to the corresponding  $\mathcal{O}(\alpha^6)$  channels, which in our case would be

$$q_1 \bar{q}_2 \rightarrow \mu^+ \mu^- e^+ \nu_e \gamma g, \quad q_1 g \rightarrow \mu^+ \mu^- e^+ \nu_e q_2 \gamma, \quad \bar{q}_1 g \rightarrow \mu^+ \mu^- e^+ \nu_e \bar{q}_2 \gamma. \quad (2.16)$$

Nevertheless, these channels are not part of our process definition, since the photon is not treated as a jet. To deal with this unsubtracted divergences, we employ the photon-to-jet conversion function introduced in Ref. [57]. In this approach, also employed in WZ scattering [16], the singularity is absorbed into the conversion function together with non-perturbative contributions, which arise when integrating over the photon virtuality down to mass scales of the light hadrons.

We move on to consider real NLO EW corrections to the  $\mathcal{O}(\alpha_s\alpha^5)$ . These corrections can be obtained in two different ways. A first contribution arises when interfering  $\mathcal{O}(g^7)$  and  $\mathcal{O}(g_s^2g^5)$  amplitudes involving a real-photon emission. The  $b\bar{b}$ - and  $\gamma\gamma$ -induced channels receive NLO QCD corrections, as discussed above, but no NLO EW corrections, since the corresponding  $\mathcal{O}(\alpha_s\alpha^5)$  vanishes owing to colour algebra. For this class of real amplitudes, an internal gluon could potentially cause an initial-state singularity from a collinear  $q \rightarrow qg$  splitting or a final-state one from a  $g \rightarrow q\bar{q}$  splitting. Nevertheless, since our signal region requires at least two jets (see Section 3) and the photon can not be promoted to a jet, these singular regions are cut away. This means that QED CS dipoles are sufficient to subtract all the IR singularities of these real terms.

A second contribution includes squared  $\mathcal{O}(g_s g^6)$  amplitudes, which correspond to the real reactions:

$$g\gamma \rightarrow \mu^+\mu^-e^+\nu_e q_1 \bar{q}_2 \gamma, \quad \gamma q_1 \rightarrow \mu^+\mu^-e^+\nu_e q_2 g \gamma, \quad \gamma \bar{q}_1 \rightarrow \mu^+\mu^-e^+\nu_e \bar{q}_2 g \gamma. \quad (2.17)$$

For the same reasons discussed above, our fiducial cuts prevent any QCD singularity in the  $g\gamma$ -induced channel, which only suffers from soft and collinear photon singularities. However, the  $\gamma q$ - and  $\gamma \bar{q}$ -induced ones require a special treatment. Whenever a soft gluon is isolated, the definition of our fiducial region removes these singular configurations, since they would lead to a mono-jet signature. The same occurs for gluons collinear to the initial/final state parton  $q_1/q_2$ . However, within the dressing procedure, any QCD parton, and so also a soft gluon, can be recombined with a hard photon. This recombination step would lead to a two-jet event with a soft-gluon singularity, which should be compensated by the virtual QCD correction to the partonic channel

$$\gamma q_1 \rightarrow \mu^+\mu^-e^+\nu_e q_2 \gamma, \quad \gamma \bar{q}_1 \rightarrow \mu^+\mu^-e^+\nu_e \bar{q}_2 \gamma. \quad (2.18)$$

Again, the latter channels are not part of our LO process definition, since photons are never considered as jets. Following the approach of Refs. [58–60], the unsubtracted singularity is removed by discarding all events with a jet that arises from the recombination of a parton  $p$  (a quark, an antiquark, or a gluon) of energy  $E_p$  with a photon of energy  $E_\gamma$  having an energy fraction  $z_\gamma = E_\gamma/(E_\gamma + E_p)$  that exceeds a cut value  $z_\gamma^{\text{cut}}$ . We have used the standard value  $z_\gamma^{\text{cut}} = 0.7$  throughout our calculation. This democratic treatment of partons to remove jets containing hard photons is not IR safe. Indeed, the cancellation of singularities from the virtual photonic corrections to the channels  $\gamma q_1 \rightarrow \mu^+\mu^-e^+\nu_e q_2 g$  and  $\gamma \bar{q}_1 \rightarrow \mu^+\mu^-e^+\nu_e \bar{q}_2 g$  is spoiled by cutting away real QED events whose collinear pair  $(q_2, \gamma)$  has  $z_\gamma > z_\gamma^{\text{cut}}$ . This artificially introduced divergence is absorbed into the quark–photon fragmentation function [61, 62]. To achieve this, the definition of the QED CS dipoles at this order is modified to include a fragmentation component and an explicit dependence on the  $z_\gamma^{\text{cut}}$  cut, as described in Refs. [58–60].

The distinction between NLO QCD corrections to  $\mathcal{O}(\alpha^6)$  and NLO EW corrections to  $\mathcal{O}(\alpha_s\alpha^5)$  that we made for the real contributions is not possible anymore for virtual ones, as has been discussed for instance in Ref. [19]. Interferences of  $\mathcal{O}(g^8)$  one-loop amplitudes

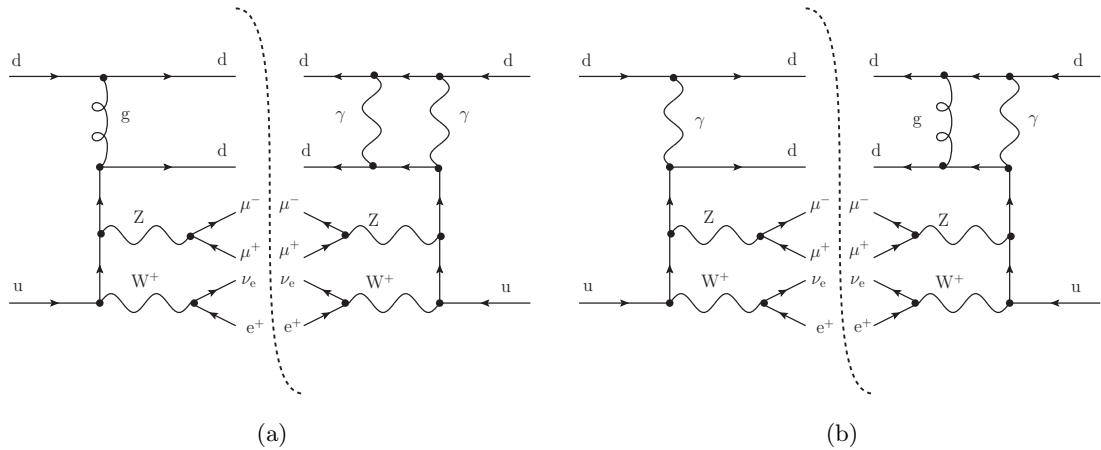


**Figure 10.** Exemplary one-loop contributions of  $\mathcal{O}(\alpha_s \alpha^6)$ . While Fig. 10(a) unambiguously corresponds to an EW correction to the  $\mathcal{O}(\alpha_s \alpha^5)$ , the contribution depicted in Fig. 10(b) can be interpreted either as a QCD correction to the  $\mathcal{O}(\alpha^6)$  or an EW correction to the  $\mathcal{O}(\alpha_s \alpha^5)$ .

with  $\mathcal{O}(g_s^2 g^4)$  tree-level ones [shown in Fig. 10(a)] can be uniquely identified as virtual EW corrections to  $\mathcal{O}(\alpha_s \alpha^5)$ . Conversely, interferences of  $\mathcal{O}(g^6)$  tree level amplitudes with  $\mathcal{O}(g_s^2 g^6)$  one-loop ones can be considered either as QCD corrections to  $\mathcal{O}(\alpha^6)$  or as EW corrections to  $\mathcal{O}(\alpha_s \alpha^5)$ , owing to the presence of a QCD–EW mixed loop, as exemplified in Fig. 10(b).

### 3 Numerical results

#### 3.1 Input parameters

In the following, we present results for the LHC at a centre-of-mass energy of 13.6 TeV. We consider the process in Eq. (2.1) with two different-flavour charged leptons in the final state and all leptons assumed to be massless. We work in the five-flavour scheme and therefore treat all light and bottom quarks as massless. A unit quark-mixing matrix is understood.

The on-shell values for the masses and widths of the EW gauge bosons are chosen according to Ref. [63],

$$\begin{aligned} M_W^{\text{OS}} &= 80.377 \text{ GeV}, & \Gamma_W^{\text{OS}} &= 2.085 \text{ GeV}, \\ M_Z^{\text{OS}} &= 91.1876 \text{ GeV}, & \Gamma_Z^{\text{OS}} &= 2.4952 \text{ GeV}, \end{aligned} \quad (3.1)$$

and then converted to their pole values by means of the relations [64]

$$M_V = \frac{M_V^{\text{OS}}}{\sqrt{1 + (\Gamma_V^{\text{OS}}/M_V^{\text{OS}})^2}}, \quad \Gamma_V = \frac{\Gamma_V^{\text{OS}}}{\sqrt{1 + (\Gamma_V^{\text{OS}}/M_V^{\text{OS}})^2}}. \quad (3.2)$$

The top-quark and Higgs-boson masses and widths are fixed as [63]

$$\begin{aligned} m_t &= 172.69 \text{ GeV}, & \Gamma_t &= 1.42 \text{ GeV}, \\ M_H &= 125.25 \text{ GeV}, & \Gamma_H &= 0.0041 \text{ GeV}. \end{aligned} \quad (3.3)$$

The EW coupling is extracted from the Fermi constant  $G_\mu$  by means of [65, 66]

$$\alpha = \frac{\sqrt{2}}{\pi} G_\mu \left| \mu_{\text{W}}^2 \left( 1 - \frac{\mu_{\text{W}}^2}{\mu_{\text{Z}}^2} \right) \right|, \quad (3.4)$$

where  $G_\mu = 1.16638 \cdot 10^{-5} \text{ GeV}^{-2}$ . Complex masses  $\mu_V^2 = M_V - i\Gamma_V M_V$  enter the  $\alpha$  definition consistently with the complex-mass scheme [51–54], where the masses of unstable particles, i.e. the EW vector bosons and the top quark, are treated as complex parameters in all parts of the computation. As a consequence, the EW mixing angle and the related couplings are complex valued as well.

For both the LO and the NLO calculation, we use NNPDF40\_nnlo\_as\_01180\_qed PDFs [67], extracted at NNLO with  $\alpha_s(M_Z) = 0.118$ . The usage of this PDF set allows us to properly account for the photon PDF. The strong coupling constant  $\alpha_s$  used in the calculation of the amplitudes matches the one used in the evolution of PDFs. The PDFs and the running of  $\alpha_s$  are obtained by interfacing MOCANLO with LHAPDF6 [68].

The QCD partons with pseudorapidity  $|\eta| < 5$  are clustered into jets by means of the anti- $k_T$  algorithm [69] with resolution radius  $R = 0.4$ . Photons are never considered as jets within our reconstruction. We assume a perfect b-jet tagging veto, which allows us to neglect all contributions with bottom quarks in the final state.

Our fiducial region is defined by a choice of selection cuts which is inspired by the HL LHC prospect studies for the ATLAS detector [14]. In particular, we require that exactly two jets pass the tagging cuts

$$p_{\text{T},j_i} > 40 \text{ GeV} \quad \text{and} \quad |y_{j_i}| < 3 \quad \text{with } i = 1, 2. \quad (3.5)$$

We remark that these requirements on the jets effectively veto any additional jet, except if it has very high rapidity or very low transverse momentum.

The two tagged jets  $j_1$  and  $j_2$  are required to fulfil

$$50 \text{ GeV} < M_{j_1 j_2} < 100 \text{ GeV}. \quad (3.6)$$

Photons are recombined with quarks and charged leptons using the anti- $k_T$  clustering algorithm using  $R = 0.1$ . For the three charged leptons, we impose the rapidity cut

$$|y_{\ell_i}| < 4, \quad (3.7)$$

where  $\ell_i$  runs over the set of charged leptons ordered by transverse momentum. The charged leptons are additionally required to satisfy

$$p_{\text{T},\ell_1} > 50 \text{ GeV}, \quad p_{\text{T},\ell_2} > 40 \text{ GeV}, \quad p_{\text{T},\ell_3} > 20 \text{ GeV}. \quad (3.8)$$

The invariant mass of the pair of opposite-sign same-flavour leptons, i.e. the  $\mu^+ \mu^-$  pair in our case, must fall into the mass window

$$76 \text{ GeV} < M_{\mu^+ \mu^-} < 106 \text{ GeV}, \quad (3.9)$$



	$\mathcal{O}(\alpha^6)$	$\mathcal{O}(\alpha_s\alpha^5)$	$\mathcal{O}(\alpha_s^2\alpha^4)$	sum
$\sigma_{\text{LO}}$ [ab]	50.230(2)	8.144(2)	847.7(5)	906.0(5)
$\Delta_{\text{tot}}$ [%]	5.54	0.90	93.56	100.00

**Table 1.** Cross sections (in ab) of  $pp \rightarrow \mu^+\mu^-e^+\nu_e jj$  at each of the leading orders. Integration errors on the last digit are given in parentheses. The cross sections include all partonic subprocesses that arise at the given order except those with one or more bottom quarks in the final state. The second row shows each LO cross section relative to the sum of the leading orders in percent.

while the positron  $e^+$  is constrained by the transverse-mass cut

$$M_{T,W^+} > 20 \text{ GeV} \quad \text{with} \quad M_{T,W^+} = \sqrt{2p_{T,e^+}p_{T,\nu_e}(1 - \cos(\phi_{e^+} - \phi_{\nu_e}))}, \quad (3.10)$$

where  $\phi$  is the azimuthal angle around the collision axis. We note that the definition of  $M_{T,W^+}$  makes use of the momentum of the neutrino  $\nu_e$  at Monte Carlo-truth level, which we employ as a definition for the missing transverse momentum.

We set the factorisation and renormalisation scales to the same central value  $\mu_0$ ,

$$\mu_F = \mu_R = \mu_0 = M_Z^{\text{OS}}. \quad (3.11)$$

### 3.2 Fiducial cross sections

To assess the signal-to-background ratio, we compare the cross sections of the different leading orders discussed in Section 2, integrated over the phase space defined by the cuts of Section 3.1. Table 1 shows these results, where we include all partonic processes that arise at the given order except those with one or more bottom quarks in the final state. The second entry of the middle row contains the LO cross section of our signal, which contributes to  $\mathcal{O}(\alpha^6)$ ,

$$\sigma_{\text{LO}}^{\text{sig}} = 50.230(2) \text{ ab}, \quad (3.12)$$

where the integration uncertainty on the last digit is given in parentheses. In the bottom row, the relative size of each order is displayed in percent. While the interference background of  $\mathcal{O}(\alpha_s\alpha^5)$  in the third column is below the percent level, it is evident that the QCD background, in the fourth column, can not be reduced by our cut setup to less than 93.6%.

We further study the signal-to-background ratio within each subprocess type. Table 2 displays the contribution at each LO of each subprocess type to our signal. For comparison, it also shows the contributions  $\sigma_{\text{LO}}^b$  of subprocesses with one or more bottom quarks in the final state, which are not part of our signal. The contribution  $\sigma_{\text{LO}}^?$  stands for either double- or single-photon-induced subprocesses, depending on the perturbative order. Below each absolute number (in ab), we show the relative size  $\Delta_{\alpha^6}$  of each contribution with respect to the total cross section of the signal in Eq. (3.12).

We observe that quark-(anti)quark-initiated subprocesses make up 97% of the cross section of our LO signal at  $\mathcal{O}(\alpha^6)$ . At  $\mathcal{O}(\alpha_s\alpha^5)$ , these subprocesses give rise to interference

Subprocess	$\mathcal{O}(\alpha^6)$	$\mathcal{O}(\alpha_s \alpha^5)$	$\mathcal{O}(\alpha_s^2 \alpha^4)$	sum
$\sigma_{\text{LO}}^{qq/\bar{q}\bar{q}/q\bar{q}}$ [ab]	48.657(2)	-2.4189(5)	59.2(1)	105.4(1)
$\Delta_{\alpha^6}$ [%]	96.87	-4.82	117.92	209.98
$\sigma_{\text{LO}}^\gamma$ [ab]	0.8592(1)	10.563(2)	-	11.422(2)
$\Delta_{\alpha^6}$ [%]	1.71	21.03	-	22.74
$\sigma_{\text{LO}}^{\text{b}\bar{\text{b}}}$ [ab]	0.7137(1)	-	0.0034516(7)	0.7171(1)
$\Delta_{\alpha^6}$ [%]	1.42	-	0.01	1.43
$\sigma_{\text{LO}}^{\text{b}/\bar{\text{b}}}$ [ab]	12.3879(6)	-	7.628(2)	20.016(2)
$\Delta_{\alpha^6}$ [%]	24.66	-	15.19	39.85

**Table 2.** Cross sections (in ab) at each of the leading orders by type of partonic subprocess of  $\mu^+\mu^-e^+\nu_e jj$  production. Here,  $q$  stands for a generic light (anti)quark in  $S_q$  [see Eq. (2.2)]. The rightmost column shows the cross section of each subprocess type summed over the leading orders. The cross section of subprocesses with at least one photon in the initial state is denoted by  $\sigma_{\text{LO}}^\gamma$ , while  $\sigma_{\text{LO}}^{\text{b}\bar{\text{b}}}$  stands for the cross section of bottom-antibottom-initiated subprocesses. For comparison, we show the cross section  $\sigma_{\text{LO}}^{\text{b}}$  of subprocesses with at least one bottom-quark in the final state, which is not part of our signal. Integration errors on the last digits are given in parentheses. The odd rows ( $\Delta_{\alpha^6}$ ) show each cross section relative to  $\sigma_{\text{LO}}^{\text{sig}}$  in Eq. (3.12).

contributions that are negative when integrated over the fiducial phase-space volume and represent less than 5% relative to our signal. On the other hand, the  $\mathcal{O}(\alpha_s^2 \alpha^4)$  contribution of  $qq/\bar{q}\bar{q}/q\bar{q}$ -induced subprocesses is larger than the one of  $\mathcal{O}(\alpha^6)$  by 21%.

Photon-induced contributions arise only at orders  $\mathcal{O}(\alpha^6)$  and  $\mathcal{O}(\alpha_s \alpha^5)$ . At the former order, only photon-photon-initiated subprocesses are present and represent 2% of the signal. At the latter order, only single-photon-initiated subprocesses exist. Contrary to the quark-(anti)quark subprocesses, their contribution arises from squared amplitudes and is as large as 21% of our signal.

Bottom-antibottom-induced subprocesses contribute at orders  $\mathcal{O}(\alpha^6)$  and  $\mathcal{O}(\alpha_s^2 \alpha^4)$ , as discussed in Section 2. At our LO signal, the  $\text{b}\bar{\text{b}}$  cross section is similar in size to that of the  $\gamma\gamma$ -induced subprocesses. In both cases the PDF suppression is compensated by the enhancement from EW resonances (see Fig. 3). That does not occur at  $\mathcal{O}(\alpha_s^2 \alpha^4)$ , where the  $\text{b}\bar{\text{b}}$  cross section is two orders of magnitude smaller.

Subprocesses with one or more bottom quarks in the final state, which we assume to be perfectly vetoed, would induce a sizeable contribution of 25% of our signal at  $\mathcal{O}(\alpha^6)$ . At  $\mathcal{O}(\alpha_s^2 \alpha^4)$ , their contribution is smaller and represents 15% of our signal cross section. This can be explained by the enhancement from top-quark resonances, which are present at  $\mathcal{O}(\alpha^6)$  but absent at  $\mathcal{O}(\alpha_s^2 \alpha^4)$ , as discussed in Section 2. As the  $\text{b}\bar{\text{b}}$ -induced subprocesses, those with one or more b quarks in the final state do not contribute to  $\mathcal{O}(\alpha_s \alpha^5)$  because of colour algebra.

Table 3 displays a more detailed decomposition of each LO, where the contributions of all different subprocess types are shown separately. To simplify this presentation, we

Subprocess	$\mathcal{O}(\alpha^6)$ [ab]	$\mathcal{O}(\alpha_s\alpha^5)$ [ab]	$\mathcal{O}(\alpha_s^2\alpha^4)$ [ab]
$q\bar{q} \rightarrow q\bar{q}$	47.616(2)	-0.4524(2)	39.1(1)
b	12.3879(6)	-	7.628(2)
$qq/\bar{q}\bar{q}$	1.04105(5)	-1.9664(4)	20.05(7)
$\gamma\gamma$	0.8592(1)	-	-
$b\bar{b}$	0.7137(1)	-	0.0034516(7)
$\gamma q/\gamma\bar{q}$	-	9.617(2)	-
$g\gamma$	-	0.9460(4)	-
gg	-	-	17.5(1)
$gq/g\bar{q}$	-	-	608.8(3)
$q\bar{q} \rightarrow gg$	-	-	162.0(1)
total	62.618(2)	8.144(2)	855.3(5)

**Table 3.** Cross sections (in ab) of all sets of partonic subprocesses contributing to each of the leading orders of  $\mu^+\mu^-e^+\nu_ejj$  production. The label  $q(\bar{q})$  stands for a generic light (anti)quark in  $S_q$ . In the last row, the sum of all partonic channels contributing at that specific order is reported. Integration errors on the last digit are given in parentheses.

include all subprocesses induced by one quark and one antiquark in the type  $q\bar{q}$  in the second row. This type thus contains both subprocesses that are compatible with a tri-boson topology, like those in Eq. (2.2), as well as subprocesses that are not, as those on the right of Eq. (2.3). The subprocess type  $qq/\bar{q}\bar{q}$  corresponds to the first two partonic process types of Eq. (2.3), which are part of the tri-boson background. They are listed separately in the fourth row of Table 3.

The second column of Table 3 confirms once more that the quark–antiquark subprocesses are responsible for most of our signal cross section. This is a consequence of our fiducial phase space, as this class of subprocesses genuinely embeds the tri-boson signature (see Section 2) and confirms that our selection cuts work as intended.

In the third column, the interference contributions of  $qq$ -,  $\bar{q}\bar{q}$ -, and  $q\bar{q}$ -induced subprocesses are both negative and of the same order of magnitude. In contrast, there is a difference between the two types of single-photon-induced subprocesses,  $\gamma q/\gamma\bar{q}$  and  $g\gamma$ , the former contribution being an order of magnitude larger than the latter. The likely reason for this is our event selection, as has been discussed in Section 2.1.2. The  $\gamma q/\gamma\bar{q}$  initial state produces a (anti)quark–gluon pair, which is more likely to be misidentified as the decay products of a vector boson than a quark–antiquark pair that is produced by  $g\gamma$ -induced subprocesses. This is because the invariant mass of the quark–gluon pair is typically smaller than the one of the quark–antiquark pair in these subprocesses.

The rightmost column of Table 3 shows that the by far largest contribution to the  $\mathcal{O}(\alpha_s^2\alpha^4)$  cross section stems from gluon–quark-induced subprocesses. It represents more than 70% of this order, followed by the quark–antiquark-induced contribution with a final-state gluon pair, which makes up 19% of the full  $\mathcal{O}(\alpha_s^2\alpha^4)$  result. As before, we attribute these large contributions to the misidentification of a  $gq/g\bar{q}$  or  $gg$  pair as a hadronically

Subprocess	$\mathcal{O}(\alpha^6)$ [ab]	$\mathcal{O}(\alpha^7)$ [ab]	$\Delta_{\alpha^6}^{(i)}$ [%]	$\mathcal{O}(\alpha_s\alpha^6)$ [ab]	$\Delta_{\alpha^6}^{(i)}$ [%]
$q\bar{q} \rightarrow q\bar{q}$	47.616(2)	-7.81(5)	-16.4	-6.83(6)	-14.3
$qq/\bar{q}\bar{q}$	1.04105(5)	-0.1156(3)	-11.1	4.19(1)	402.5
$\gamma\gamma$	0.8592(1)	-0.1045(6)	-12.1	-0.1341(4)	-15.6
$b\bar{b}$	0.7137(1)	-0.0836(4)	-11.7	-0.2195(5)	-30.7
$\gamma q/\gamma\bar{q}$	-	0.9175(2)	-	-0.593(6)	-
$g\gamma$	-	-	-	0.0053(7)	-
$gq/g\bar{q}$	-	-	-	5.766(3)	-
total	50.230(2)	-7.20(5)	-14.3	2.17(6)	4.3

**Table 4.** Total and relative NLO cross sections (in ab) for different types of partonic subprocesses contributing to  $\mu^+\mu^-e^+\nu_{ejj}$  production at the LHC. The second column shows the LO signal from Table 3 for reference. The third and fifth columns list the NLO EW and QCD corrections, respectively. The fourth and sixth columns show the NLO corrections relative to the LO signal of each subprocess type from the second column. In the last line, the sum of all partonic channels contributing at that specific order is reported. Integration errors on the last digit are given in parentheses.

decaying vector boson. Gluon–gluon-induced subprocesses, which are expected to be enhanced by their PDFs, produce a final-state quark pair that is misidentified less often owing to its large invariant mass (see Section 2.1.3), which likely leads to the relatively small contribution of 17.5 ab. All other subprocesses that contribute at this order have no external gluons but proceed by the exchange of an internal gluon as mentioned in Section 2. The corresponding lack of any enhancement mechanism for these latter channels offers a possible explanation for the difference in size between the  $q\bar{q}$ -induced subprocesses with  $gg$  and  $q\bar{q}$  final states.

Table 4 displays all the EW and NLO QCD corrections that we calculated. As before, these results are decomposed by type of subprocess. The second column reproduces the LO signal results from Table 3 for comparison. To the right of each absolute NLO correction, we give its size  $\Delta_{\alpha^6}^{(i)}$  relative to the  $\mathcal{O}(\alpha^6)$  cross section of the same subprocess type.

The  $q\bar{q}$ -induced subprocesses receive the largest EW contributions, which amount to -16.4% of the corresponding leading order and -15.5% of the total  $\mathcal{O}(\alpha^6)$  cross section. The rest of the subprocess types gets relative EW corrections of -12%, which are nevertheless below the percent level with respect to the total LO signal cross section. The  $\mathcal{O}(\alpha^7)$  cross section of photon–quark-induced subprocesses, for which no contribution at  $\mathcal{O}(\alpha^6)$  exists, amounts to about +1.8% of our full LO signal. All in all, our process receives relative EW corrections of -14.3%, which is almost as large as for the same final state in the VBS phase space [16].

In previous studies, it has been found for several tri-boson production processes that the quark-induced and photon-induced NLO EW contributions of order  $\mathcal{O}(\alpha^7)$  can be individually large but often cancel against each other to yield more modest total NLO EW corrections. In Ref. [26], where the on-shell production of  $W^+W^-Z$  at the LHC was

studied, a relative EW correction of  $-8.8\%$  was reported for the quark-induced channels and  $+6.8\%$  for the photon-quark-induced ones. Relative EW corrections have been calculated for WWW production with different final states. In Ref. [27], the on-shell process was investigated and the values  $-4.17\%$  and  $+11.46\%$  for quark- and photon-quark-induced contributions were found. The off-shell process with fully leptonic final state was studied in Ref. [33] for two different cut setups. There, for the relative EW corrections from quark- and photon-quark-induced contributions, respectively, the values  $-8.5\%$  and  $+2.4\%$  were obtained for one setup (Table 2), while the values  $-7.8\%$  and  $+7.78\%$  were found for the other setup (Table 4). The semi-leptonic final state of WWW production was investigated in Ref. [34], where for the quark- and photon-quark-induced corrections the values  $-7.2\%$  and  $+2.6\%$  were found.

The extent of the cancellation between quark- and photon-quark-induced contributions at  $\mathcal{O}(\alpha^7)$  appears to be cut dependent. For the process studied in this article, it is not substantial, as mentioned above. On the other hand, the relative contribution of quark-induced processes at  $\mathcal{O}(\alpha^7)$  that we find exceeds the values in the literature for related tri-boson processes. Large negative EW corrections at high energies typically arise from large EW Sudakov logarithms. In our setup, the mean partonic centre-of-mass energy  $\langle\sqrt{\hat{s}}\rangle$  ranges between 700 and 770 GeV for some of the most significant partonic channels. In contrast, this quantity turns out to be between 440 and 600 GeV in WWW production with a semi-leptonic final state using the setup of Ref. [34]. The comparatively high value of  $\langle\sqrt{\hat{s}}\rangle$  in our setup is at least partly due to our selection cuts, as we have confirmed by varying them. While no single cut is responsible for the large  $\langle\sqrt{\hat{s}}\rangle$ , the relatively high lower bounds on the transverse momenta and invariant masses enhance the average partonic centre-of-mass energy. In contrast to the typically large corrections of  $-15\%$  for VBS processes [15–18], the corrections of  $-14\%$  for  $W^+Zjj$  production considered here cannot be reproduced by a simple Sudakov approximation neglecting angular-dependent logarithms. Such an approximation would in fact result in even larger EW corrections. Obviously, the Sudakov limit, where all invariants are large compared to  $M_W^2$ , is not dominant in the relevant phase space for the considered process.

Turning back to Table 4, the  $\mathcal{O}(\alpha_s\alpha^6)$  correction to the  $q\bar{q}$ -induced subprocesses is similar in size to the corresponding EW correction and also negative. For  $qq/\bar{q}\bar{q}$ -induced subprocesses, we find a very large, positive QCD correction of about 400% with respect to the  $\mathcal{O}(\alpha^6)$  cross section of this subprocess type. As mentioned in Section 2,  $qq/\bar{q}\bar{q}$ -induced subprocesses are not compatible with genuine tri-boson contributions and are efficiently suppressed in our setup at LO. The large  $\mathcal{O}(\alpha_s\alpha^6)$  contribution is caused by bypassing our selection cuts, via the radiation of real gluons (see Section 2.2.2). When an additional final-state gluon is present and well separated from the other two QCD partons [see Eq. (2.13)], it can be misidentified as one of the two tagging jets coming from the hadronic decay of a vector boson (see also Ref. [34]). If the third QCD parton has a large rapidity and low enough transverse momentum, it is not tagged and the event is not dismissed by our requirement of exactly two tagged jets (see also Section 2.2.2).

Channels induced by two photons receive an  $\mathcal{O}(\alpha_s\alpha^6)$  correction of  $-16\%$  and bottom-antibottom-induced subprocesses an even larger one at  $-31\%$ . In both cases, the  $\mathcal{O}(\alpha_s\alpha^6)$

correction represents less than a percent of the full LO signal. We investigate the QCD corrections to the  $b\bar{b}$ -induced subprocesses in more detail because of their large relative size. We begin by comparing the subprocesses  $b\bar{b} \rightarrow \mu^+\mu^-e^+\nu_e c\bar{s}$  and  $d\bar{d} \rightarrow \mu^+\mu^-e^+\nu_e c\bar{s}$ , whose matrix elements differ by the presence of top-quark propagators that arise only for the former subprocess. While the real and dipole contributions are similar for both subprocesses relative to the corresponding LO, the relative virtual contributions differ substantially. When artificially setting the top-quark mass to zero in the  $b\bar{b}$ -induced subprocesses, the relative real and dipole contributions remain almost unaffected, but the relative virtual contribution significantly changes. Thus, the large relative QCD corrections to the  $b\bar{b}$ -induced subprocesses are due to top-mass effects in the virtual amplitudes.

Finally, the initial states  $\gamma q/\gamma\bar{q}$ ,  $g\gamma$ , and  $gq/g\bar{q}$  appear as real-correction subprocesses at  $\mathcal{O}(\alpha_s\alpha^6)$ . The contribution of the latter is positive and amounts to 11.5% of the total LO signal, while the former two are below the percent level. The substantial cancellations that occur at this order yield an  $\mathcal{O}(\alpha_s\alpha^6)$  correction of altogether +4.3%.

### 3.3 Differential cross sections

In this subsection, we present differential results for the process  $pp \rightarrow \mu^+\mu^-e^+\nu_e jj$  at orders  $\mathcal{O}(\alpha^6)$ ,  $\mathcal{O}(\alpha^7)$ , and  $\mathcal{O}(\alpha_s\alpha^6)$ . From now on, LO will refer to the contribution of  $\mathcal{O}(\alpha^6)$ , while NLO EW and NLO QCD denote contributions of  $\mathcal{O}(\alpha^6) + \mathcal{O}(\alpha^7)$  and  $\mathcal{O}(\alpha^6) + \mathcal{O}(\alpha_s\alpha^6)$ , respectively. We call the combination  $\mathcal{O}(\alpha^6) + \mathcal{O}(\alpha^7) + \mathcal{O}(\alpha_s\alpha^6)$  total NLO. We remark that NLO QCD quantities also contain EW corrections to the non-signal LO  $\mathcal{O}(\alpha_s\alpha^5)$ . Furthermore, only the subprocess types listed in Table 4 are taken into account and are labelled here with the same notation.

We begin our discussion with the differential cross sections with respect to the partonic centre-of-mass energy  $\sqrt{\hat{s}}$  in Fig. 11. While this quantity is not experimentally accessible, its study offers insights into the individual contributions of each subprocess type.

On the left plot, the  $\mathcal{O}(\alpha^6)$  cross section is shown in blue, decomposed in the contributions from different types of partonic subprocesses. The middle and bottom panels display the relative sizes of each contribution in percent, zoomed into separate ranges for visibility. On this plot, we recognise the dominance of the  $q\bar{q}$ -induced subprocesses that we observed at the integrated level in Section 3.2 but also find that it becomes less pronounced at higher values of the partonic centre-of-mass energy. The relative size of the  $q\bar{q}$  contribution decreases from 98% at low energies to 85% at 4 TeV. To make up for it, the  $\gamma\gamma$ - and  $qq/\bar{q}\bar{q}$ -induced relative contributions grow to more than 10% and just below 5% in the same energy range, respectively. While the growth of the relative  $\gamma\gamma$  contribution can be attributed to the photon PDF, we interpret the rise of the relative  $qq/\bar{q}\bar{q}$  contribution as a decrease in efficiency of our tri-boson selection cuts in favour of VBS contributions.

We turn to the right plot of Fig. 11. On its top panel, the NLO EW and QCD cross sections are shown separately (in green and red, respectively) and combined (in orange). We observe large negative QCD corrections in the first three bins up to 450 GeV. While the LO curve is positive in the second bin, between 150 and 300 GeV, the NLO QCD curve is in fact negative (not visible owing to the logarithmic scale). Furthermore, there is a gap between these curves of one order of magnitude in the bin between 300 and 450 GeV.

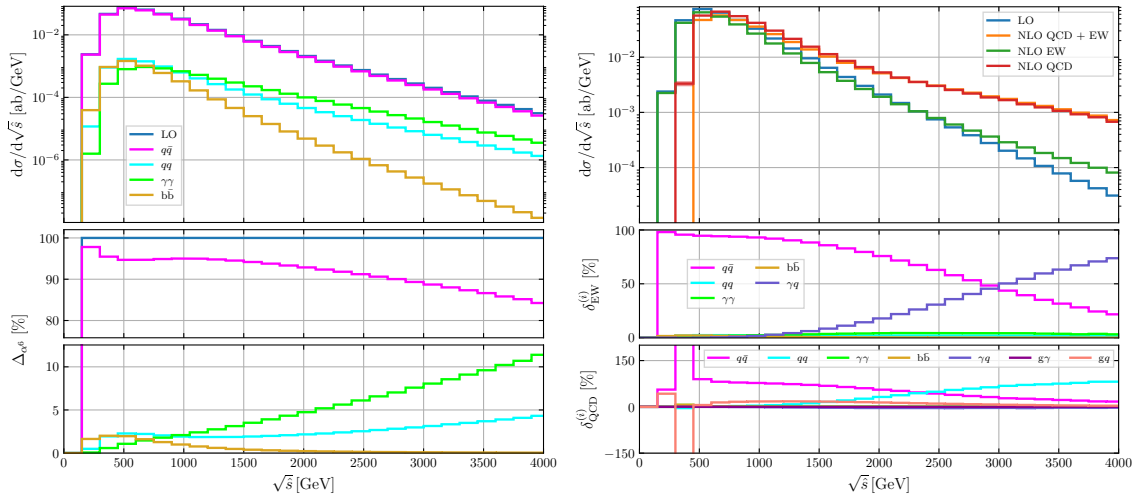


**Figure 11.** Distributions of the partonic centre-of-mass energy,  $\sqrt{\hat{s}}$ , at LO  $\mathcal{O}(\alpha^6)$  (left) and NLO  $\mathcal{O}(\alpha^6) + \mathcal{O}(\alpha^7)$  and  $\mathcal{O}(\alpha^6) + \mathcal{O}(\alpha_s \alpha^6)$  (right) decomposed into the contributions of different subprocess types. See text for details about the lower panels.

After the fourth bin, these corrections turn positive and continue growing towards higher energies, where the NLO QCD distribution significantly exceeds the LO one.

We attribute the large QCD corrections at low partonic energies,  $\langle\sqrt{\hat{s}}\rangle \lesssim 500$  GeV, to the phase-space suppression of the real contribution close to the on-shell threshold, given by  $2M_W + M_Z \approx 250$  GeV and the lack of cancellations between the real and virtual corrections. As can be seen in the upper right panel of Fig. 11, the cross section is dominated by the Born-like contributions below 500 GeV, which include integrated and subtraction dipoles and virtual corrections, and are mostly supported in the low-energy regime. The real corrections mainly contribute at higher energies, where there is more phase space available for the real emission. Furthermore, we find that  $gq/g\bar{q}$ -initiated subprocesses, which arise at  $\mathcal{O}(\alpha_s \alpha^6)$ , have a large and negative<sup>2</sup> cross section in the third bin, and significantly contribute to the observed gap.

The EW corrections are smaller, and the NLO EW distribution follows the LO curve more closely. Again, the corrections are negative at lower energies but fairly small in the first bins, as opposed to their QCD counterpart. Although the phase-space suppression of the real contribution also occurs in this case, its effect is smaller owing to the difference between the EW and QCD couplings. The EW corrections become positive at around 2300 GeV, after which the NLO EW differential cross section departs from the LO one as the energy grows.

The tails of the NLO QCD and EW distributions also behave differently. While the NLO EW curve shows a more uniformly falling tail, a change is visible in the rate at which the NLO QCD distribution diminishes after about 2 TeV. This behaviour can be traced

<sup>2</sup>The  $gq/g\bar{q}$ -contribution can be negative owing to the collinear counterterm necessary to cancel initial-state infrared divergences.

back to the real contributions of subprocesses of the  $qq/\bar{q}\bar{q}$  type, which can bypass our cuts and become more important at larger energies, slowing down the decay of the NLO QCD distribution (see also Section 2.2.2). All in all, the total NLO distribution is dominated by the QCD correction starting at around 500 GeV.

The middle and bottom right panels of Fig. 11 display the relative NLO EW and QCD cross sections of each subprocess type  $i$ , defined as

$$\delta_{\text{EW/QCD}}^{(i)} = \frac{\sigma_{\text{LO}}^{(i)} + \delta\sigma_{\text{NLO EW/QCD}}^{(i)}}{\sigma_{\text{LO}}^{\text{tot}} + \delta\sigma_{\text{NLO EW/QCD}}^{\text{tot}}}. \quad (3.13)$$

Here,  $\sigma_{\text{LO}}^{(i)}$  and  $\delta\sigma_{\text{NLO}}^{(i)}$  stand for the LO cross section of the  $i$ -th subprocess type and the corresponding NLO correction, which contains only the higher-order contribution. The superscript “tot” refers to the sum over  $i$ .

The middle panel on the right shows that the NLO EW correction is dominated by contributions of  $q\bar{q}$  type for energies below 3 TeV, while  $\gamma q/\gamma\bar{q}$  contributions become larger for higher energies. We attribute this behaviour to the high-energy enhancement of the photon PDF. This contribution is responsible for the rise of the NLO EW above the LO in the upper right plot. Relative contributions to other subprocess types do not exceed 5% in the shown range.

On the bottom panel of the right plot in Fig. 11, we observe an interesting behaviour in the third bin, between 300 and 450 GeV. There, the relative NLO cross section  $\delta_{\text{QCD}}^{(q\bar{q})}$  is 364%, while  $\delta_{\text{QCD}}^{(gq)}$  is  $-274\%$  (not visible in the plot). These large values are ultimately due to the large and negative NLO QCD corrections, visible on the top panel, which lead to a relatively small denominator in Eq. (3.13) for that bin. The rise of the QCD corrections for large  $\langle\sqrt{\hat{s}}\rangle$  is due to real gluon corrections that evade the invariant-mass cut in Eq. (3.6).

We continue by presenting some observables that are relevant for tri-boson studies. Figures 12–15 display a selection of differential distributions at the calculated leading and next-to-leading orders. In each case, the top panel of the left plot displays the distribution at each LO as well as their sum (dark magenta). Whenever a linear scale is used, the curves of  $\mathcal{O}(\alpha^6)$  (blue) and  $\mathcal{O}(\alpha_s\alpha^5)$  (salmon) are rescaled for visibility. If present, the rescaling factor is specified in the legend. The QCD background is depicted in yellow. In the lower panel, the left plots show the relative contributions of each order in percent, zoomed into separate ranges for visibility. The right plots contain distributions for the LO signal (blue) as well as the corresponding corrections at NLO EW (green), NLO QCD (red), and total NLO (orange). The relative NLO corrections in the middle and bottom panels are defined as

$$\delta = \frac{\delta\sigma_{\text{NLO EW/QCD}}}{\sigma_{\text{LO}}}, \quad (3.14)$$

where  $\sigma_{\text{LO}}$  includes only contributions of  $\mathcal{O}(\alpha^6)$ .

We begin by considering jet observables. The upper row of Fig. 12 shows the distribution in  $\Delta\phi_{j_1j_2}$ , the azimuthal angle between the tagged jets. These jets mostly originate from the decay of a vector boson. Therefore, in the laboratory frame we expect them to have a small angular separation, resulting in an enhancement of the  $\Delta\phi_{j_1j_2}$  distribution



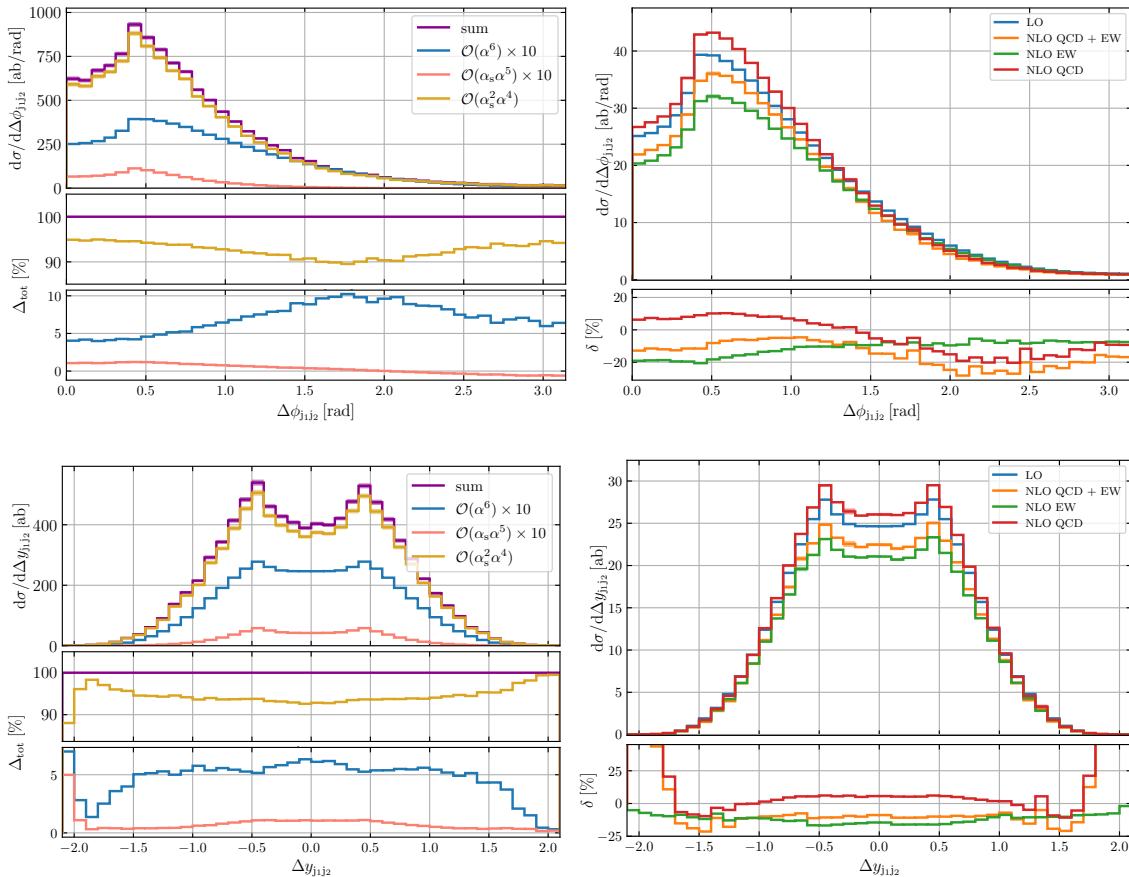


**Figure 12.** Distributions in the azimuthal angle between the tagged jets,  $\Delta\phi_{j_1 j_2}$ , (top row) and their rapidity difference,  $\Delta y_{j_1 j_2}$ , (bottom row) at LO (left column) and NLO (right column). See the main text for a description of the individual plots.

towards smaller values. Indeed, on the upper panel of the left plot, all distributions rise towards smaller angle differences but peak at around 0.4. This is related to the  $R$ -parameter of our jet-clustering algorithm. At LO, the requirement of two tagging jets can only be fulfilled if the distance

$$\Delta R_{j_1 j_2} = \sqrt{\Delta\phi_{j_1 j_2}^2 + \Delta y_{j_1 j_2}^2} \quad (3.15)$$

between them in the  $\phi$ - $y$  plane is larger than 0.4, which effectively acts as a cut. If  $\Delta\phi_{j_1 j_2} < 0.4$ , then Eq. (3.15) forces  $\Delta y_{j_1 j_2}$  to assume larger values, reducing the available phase-space volume. As visible in the lower left panel, the relative contribution of the  $\mathcal{O}(\alpha^6)$  varies between 4% and 10% with a maximum near  $\Delta\phi_{j_1 j_2} = 1.75$ , while the relative interference contribution of order  $\mathcal{O}(\alpha_s \alpha^5)$  falls from 1.2% to  $-0.6\%$  at  $\Delta\phi_{j_1 j_2} = \pi$ . Accordingly the dominant  $\mathcal{O}(\alpha_s^2 \alpha^4)$  varies between 95% and 89%.

The shapes of the absolute NLO distributions of  $\Delta\phi_{j_1 j_2}$  on the upper panel of the top right plot of Fig. 12 are similar to the LO distribution. On the bottom panel, we recognise a difference in behaviour between NLO EW and QCD corrections. While the former is consistently negative and decreases in size from  $-21\%$  to  $-7\%$  towards higher values of

$\Delta\phi_{j_1j_2}$ , the QCD correction amounts to 6% at  $\Delta\phi_{j_1j_2} = 0$ , grows to 10% at 0.6, where the bulk of the cross section sits, and then goes down to  $-20\%$  for  $\Delta\phi_{j_1j_2} \gtrsim 2$ . Since the NLO EW corrections are larger than the QCD ones in the bulk of the distribution, the total NLO correction ranges between  $-5\%$  and  $-28\%$ .

The lower row of Fig. 12 shows the distribution in the rapidity difference between the tagged jets  $\Delta y_{j_1j_2}$ . The distribution is symmetric with two peaks at  $\pm 0.4$  as in the  $\Delta\phi_{j_1j_2}$  distribution. The relative contribution of the  $\mathcal{O}(\alpha^6)$  amounts to 5–6% and the interference contribution reaches at most 1%. The relative QCD and EW corrections, in the right plot, are rather flat where the distribution is sizeable. For rapidity differences larger than 1.7, the QCD correction becomes large, reaching close to 300% at  $\Delta y_{j_1j_2} = \pm 2$  (not visible in the figure). This behaviour is not unexpected, since contributions compatible with VBS, for which larger rapidity differences are typical, can evade our tri-boson selection cuts at  $\mathcal{O}(\alpha_s\alpha^6)$  via the real emission, as discussed in Section 2.2.2. The distributions in  $\Delta y_{j_1j_2}$  vanish for values larger than 2.1 as a consequence of the cuts in Eqs. (3.5) and (3.6) on  $M_{j_1j_2}$  and  $p_{T,j_i}$ , which constrain the value of  $\Delta y_{j_1j_2}$  according to Eq. (49.45) of Ref. [63]

$$M_{j_1j_2}^2 = 2 p_{T,j_1} p_{T,j_2} (\cosh \Delta y_{j_1j_2} - \cos \Delta\phi_{j_1j_2}) . \quad (3.16)$$

Figure 13 shows in its upper row the distribution in the invariant mass of the tagged-jet pair  $M_{j_1j_2}$ . On the left plot, the LO signal clearly displays the expected peaks at the W- and Z-boson masses, which are even visible in the sum of leading orders. The QCD background slightly increases with growing invariant mass, while the interference contribution tends to decrease with two steps at the vector-boson masses. The lower panel shows that the LO signal represents 38% of the total LO cross section at the W-boson peak and 14% at the Z-boson peak. The interference contribution remains below 1.5% in the whole considered range. On the right plot, the left flanks of both peaks receive large, positive QCD corrections of up to 1000% (note that the curves for the real QCD correction is scaled down by a factor 100). The peaks themselves are reduced and slightly shifted towards lower values in the NLO QCD distribution, and the first bins to the right of each peak centre have negative QCD corrections. This radiative-return effect is well known and due to the real gluon emission from a tagged jet. If the gluon is well separated, it carries away some of the energy from the products of the hadronically decaying vector boson, resulting in a smaller invariant mass of the tagged jets. The right flank of the Z-boson peak receives substantial positive QCD corrections. These are also driven by the additional real radiation, which can influence the jet identification and thereby increase the likelihood for the invariant mass of the tagged jets to be further above the Z-boson resonance [17, 34, 70]. Specifically, the extra QCD parton can be tagged as a jet, while the other tagging jet results from the recombination of the weak-boson decay products into a single jet, shifting the resonant contributions to higher invariant masses. Alternatively, the extra real parton and one quark from the vector-boson decay may be recombined into a tagged jet, while the other quark from the decay is tagged as the other jet.

The behaviour of the NLO EW distribution is significantly different. It is consistently negative and takes its largest value of  $-17\%$  at the W peak. The radiative-return effect owing to unclustered real-photon radiation is moderate for the distribution in  $M_{j_1j_2}$ . This

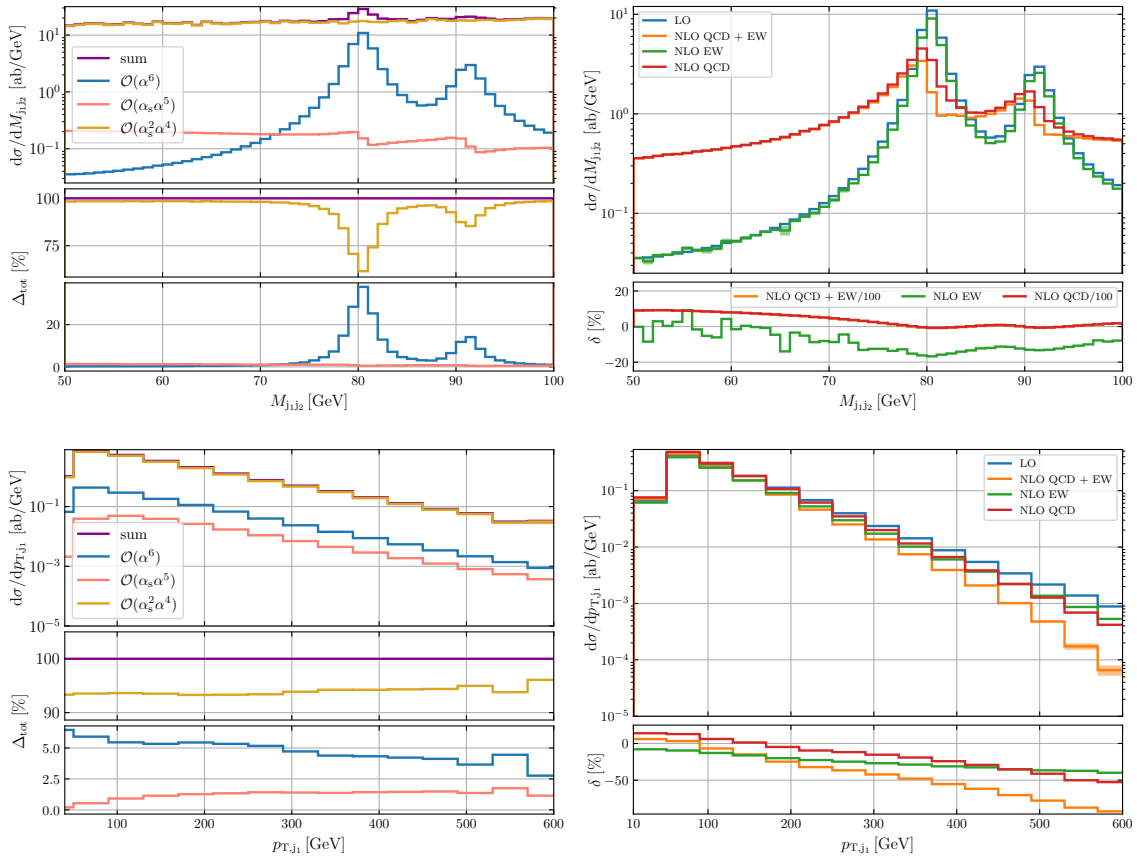


**Figure 13.** Distributions in the invariant mass of the tagged-jet pair,  $M_{j_1 j_2}$ , (top row) and the transverse momentum of the hardest tagged jet,  $p_{T, j_1}$ , (bottom row).

is due to the smallness of the EW coupling relative to the strong coupling and the relative smallness of the quark charges with respect to the lepton charges.

The distribution in the transverse momentum of the hardest jet,  $p_{T, j_1}$ , is shown on the lower row of Fig. 13. At LO, the relative contribution of the LO signal decreases with growing  $p_T$  from 6.4% to 2.6% at  $p_{T, j_1} = 600$  GeV, while the LO interference grows from 0.2% to 1.8%. Although the relative total NLO correction (right plot) amounts to only 6% for small transverse momenta, it significantly influences the tail of the distribution, reaching  $-87\%$  at 600 GeV. The relative EW correction varies from  $-8\%$  to  $-37\%$  with increasing transverse momentum. This increase in size towards higher energies is driven by the large EW Sudakov logarithms mentioned in Section 3.2. The QCD correction falls from positive values at small transverse momentum down to  $-52\%$  at 600 GeV. We attribute these large negative QCD corrections at high transverse momenta to our choice of a fixed scale at a low value [cf. Eq. (3.11)]. The appearance of large negative EW and QCD corrections is common to all distributions for high transverse momenta or invariant masses.

We now examine distributions in observables related to the charged leptons. On the top row of Fig. 14, we present the distribution in the cosine of the angle between the

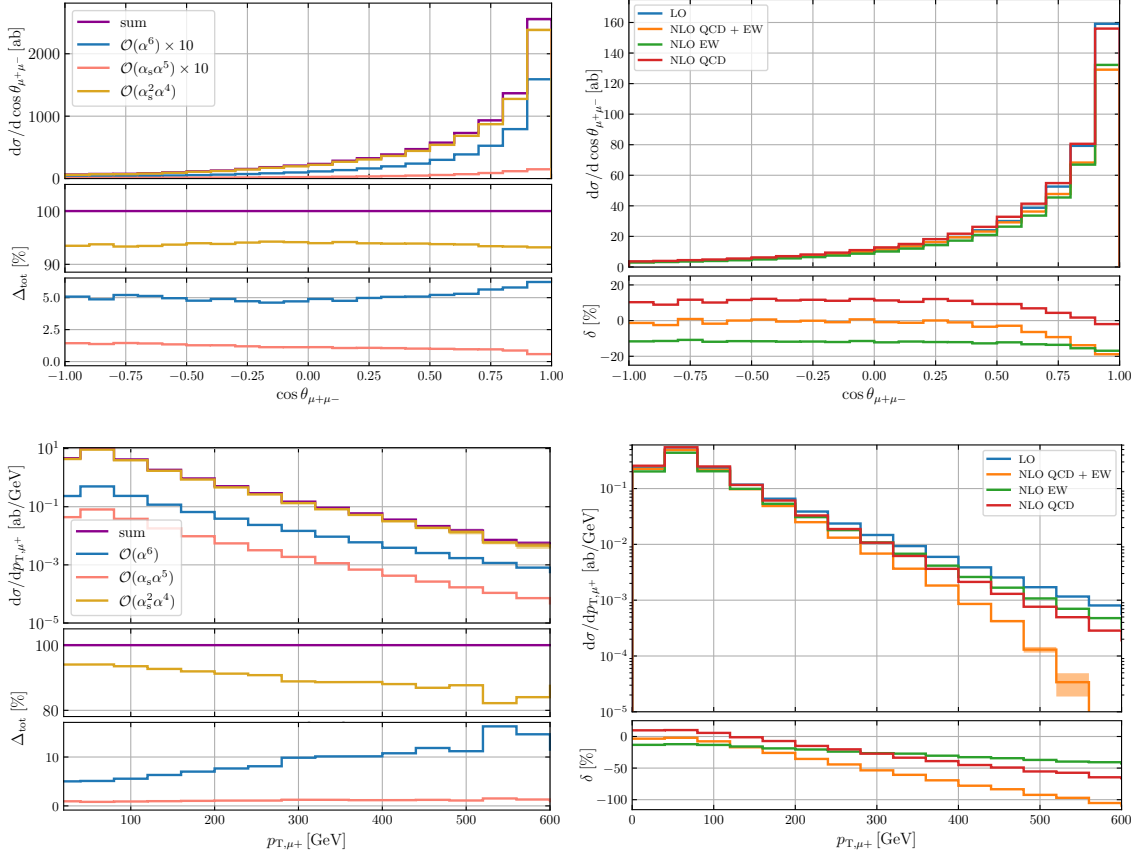


**Figure 14.** Distributions in the cosine of the opening angle between the muon and antimuon,  $\cos\theta_{\mu+\mu^-}$ , (top row) and the transverse momentum of the antimuon,  $p_{T,\mu^+}$ , (bottom row).

muon and the antimuon,  $\cos\theta_{\mu+\mu^-}$ . Both the left and the right plots display similar behaviours for all curves, with a small opening angle being preferred in all cases. The relative LO differential cross sections in the lower panel to the left do not vary by more than 2%. The relative NLO EW correction on the lower right panel is between  $-10.5\%$  and  $-12\%$  in the range from  $-1$  to  $0.5$  but increases in size towards  $\theta_{\mu+\mu^-} = 0$  reaching  $-17\%$  in the rightmost bin. This results from the fact that at higher energies, where the EW Sudakov corrections are large, the Z bosons are more boosted, leading to more collinear muon–antimuon pairs. The QCD correction remains between  $9\%$  and  $12\%$  for  $\cos\theta_{\mu+\mu^-}$  within  $-1$  and  $0.6$ . Towards larger values, it falls and becomes  $-2\%$  in the last bin, again because this region is dominated by contributions from high scattering energies. Up to  $\cos\theta_{\mu+\mu^-} \approx 0.4$ , the EW and QCD corrections largely cancel giving a total NLO correction between  $-2.5\%$  and  $0.7\%$ . Thereafter, the total NLO correction is dominated by EW corrections and almost reaches  $-19\%$  in the last bin.

The distribution in the transverse momentum of the antimuon is shown on the lower row of Fig. 14. The relative  $\mathcal{O}(\alpha^6)$  contribution grows towards larger energies from  $5\%$  to  $15\%$ , while the one of  $\mathcal{O}(\alpha_s^2\alpha^4)$  decreases from  $94\%$  to  $84\%$ . The total relative NLO

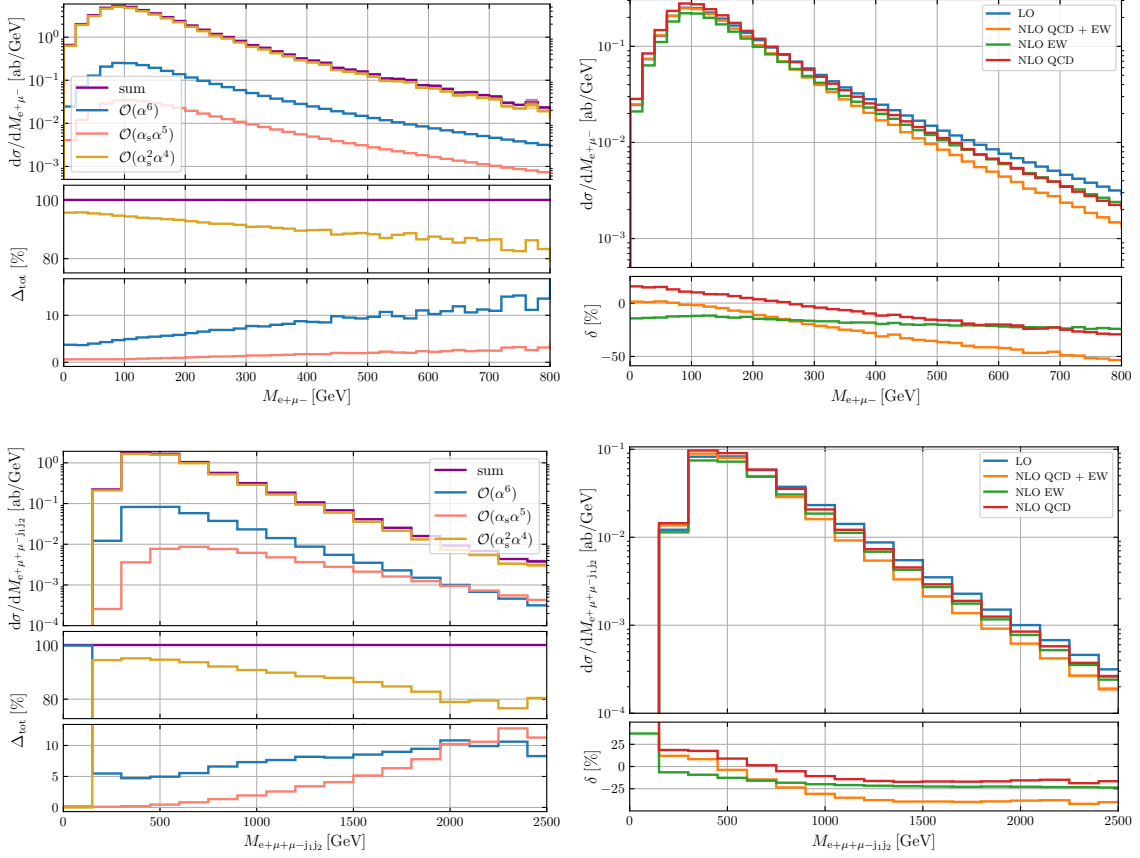


**Figure 15.** Distribution in the invariant mass of the positron–muon system,  $M_{e+\mu^-}$  (upper row), and the invariant mass of the system composed of all visible particles,  $M_{e+\mu^+\mu^-j_1j_2}$ , (bottom row).

corrections behave similar to those of the  $p_{T,j_1}$  distribution. They range between  $-2\%$  and  $-4\%$  at low transverse momenta but become large in the tail, and even reach  $-105\%$  for  $p_{T,\mu^+} = 600$  GeV. The EW correction grows in size from  $-13\%$  to  $-41\%$  with increasing transverse momentum. The QCD correction is  $+10\%$  at small  $p_{T,\mu^+}$  and then becomes negative with increasing  $p_{T,\mu^+}$  to reach  $-64\%$  at 600 GeV.

We turn to Fig. 15, which shows the distribution in the invariant mass of the positron–antimuon system  $M_{e+\mu^-}$  on its upper row. On the lower panel of the left plot, the LO signal increases from  $3.6\%$  at small invariant masses to  $14\%$  at 800 GeV, while the interference grows from  $0.6\%$  to  $3.1\%$  in the same invariant-mass range. On the right plot, the positive QCD correction and the negative EW correction approximately cancel to give a total positive relative NLO correction of at most  $2\%$  in the range below 100 GeV, where the peak of the distribution is located. For larger values, the total NLO correction becomes negative owing to the decrease of the QCD correction, which itself turns negative at around 250 GeV. As a consequence, the tail of the distribution obtains a significant suppression and the total NLO correction amounts to  $-53\%$  at 800 GeV. The relative EW correction only slightly varies from  $-12\%$  to  $-24\%$  in the tail.

We finish our discussion with the lower row of Fig. 15, which displays the distribution in the invariant mass of all visible final-state particles,  $M_{e^+\mu^+\mu^-j_1j_2}$ . As in other LO results, the relative QCD background decreases towards larger mass values, and in this case falls to 76% at  $M_{e^+\mu^+\mu^-j_1j_2} = 2.5$  TeV. Correspondingly, the LO signal increases from 5% to 8% and the interference from 0% to 13%. This is the only observable that we found, where the  $\mathcal{O}(\alpha_s\alpha^5)$  contribution exceeds the LO signal in parts of phase space (above 2 TeV). At NLO, both types of corrections follow a similar trend. For lower values of the invariant mass, both the QCD and the EW correction are positive. They both diminish for larger invariant masses, and end up being both negative and similar in size towards the upper limit of the shown range. In the tail of the distribution, the total NLO correction reaches  $-42\%$ .

## 4 Conclusions

In this work we presented a calculation for the process  $pp \rightarrow \mu^+\mu^-e^+\nu_e jj$  at the LHC at 13.6 TeV in a phase space constructed to enhance the tri-boson-production mechanism. The same process was studied in Ref. [16] in a VBS-like phase space.

We computed the complete set of LO contributions. They comprise the  $\mathcal{O}(\alpha^6)$ , which is the only one that includes the tri-boson signal, and the  $\mathcal{O}(\alpha_s\alpha^5)$  and  $\mathcal{O}(\alpha_s^2\alpha^4)$ , which are part of the background. Additionally, we evaluated NLO corrections at  $\mathcal{O}(\alpha^7)$  (NLO EW) and  $\mathcal{O}(\alpha_s\alpha^6)$  (NLO QCD). We point out that the latter contribution, which we refer to as the QCD correction to our LO signal, also receives EW corrections to the  $\mathcal{O}(\alpha_s\alpha^5)$ . All resonant and non-resonant effects, together with interference terms, have been exactly retained. All partonic channels relevant for the description of the tri-boson signal have been taken into account, including the photon- and  $\bar{b}b$ -induced ones. In our calculation we only excluded partonic channels with bottom quarks in the final state by assuming a perfect b-jet tagging and veto. These channels can induce a top-quark resonance and highly contaminate our signal, as was confirmed by evaluating them at LO. We found that they amount to roughly 25% and 15% of the  $\mathcal{O}(\alpha^6)$  at  $\mathcal{O}(\alpha_s\alpha^5)$  and  $\mathcal{O}(\alpha_s^2\alpha^4)$ , respectively.

We presented results for the fiducial cross section and differential distributions. At the inclusive level we performed a thorough study of the individual contributions of the different partonic channels at the different perturbative orders. When considering corrections to the  $\mathcal{O}(\alpha^6)$ , the LO signal, NLO EW corrections amount to  $-14\%$ , and receive contributions predominantly from quark-antiquark- and photon-quark-induced channels. These corrections are considerably larger than those found for other tri-boson processes in previous calculations [26, 27, 32–34], and as sizeable as the NLO EW corrections to the process in a VBS-prone acceptance region [16]. This is in contrast to the outcome of Ref. [34], where EW corrections to  $pp \rightarrow \mu^+\nu_\mu e^+\nu_e jj$  were found to be much smaller in a tri-boson-prone signal region than in a VBS-prone one. We attribute this to the comparably high average partonic centre-of-mass energy of our process, which is partly due to the chosen setup, which enhances the size of the EW corrections through large EW logarithms of Sudakov type. On the other hand, NLO QCD corrections are moderate at the integrated level and amount to 4% of the LO signal.

At the differential level both NLO EW and QCD corrections can become sizeable and show an interesting interplay for most of the observables that we studied. Not only does their inclusion affect the normalisation of the predictions of the LO signal, but it also leads to relevant shape effects. For the majority of the phase-space regions where the bulk of the cross section resides, the two corrections have opposite signs. Specifically, NLO EW corrections are negative and for angular observables, like the azimuthal angle or rapidity difference of the tag jets, larger in absolute value than the corresponding QCD ones. In the considered transverse-momentum and invariant-mass distributions, we observed large cancellations between the two corrections in the most-populated phase-space regions. For this second class of observables we saw that NLO EW corrections stay negative when moving to high-energy values, with a growth in size driven by large EW Sudakov logarithms and can reach  $-40\%$  in the considered phase-space regions. On the other hand, the NLO QCD contributions change sign towards the tails of these distributions, providing an additional source of large and negative corrections which can amount up to  $-60\%$ . This latter behaviour is understood as an artifact of the choice the  $W$ -boson mass as a fixed renormalisation scale that is small compared to the energy scales in the distribution tails.

With this work we presented new results for  $pp \rightarrow \mu^+ \mu^- e^+ \nu_e jj$  in a phase-space region that by now has received little attention from the theory community, and we provided one more study of the triple-vector-boson-production mechanism for a completely new final state. The importance of this process in consolidating our knowledge of the SM and in constraining new-physics scenarios is established. The improved theoretical control on this process will potentially be a crucial ingredient for the experimental analyses in the upcoming High-Luminosity stage of the LHC.

## Acknowledgements

The authors are indebted to Christopher Schwan for useful discussions and to Mathieu Pellen for some clarifications about the results of Ref. [16]. We would like to thank Saptaparna Bhattacharya and Andrea Sciandra for fruitful discussion on CMS and ATLAS tri-boson analyses. This work is supported by the German Federal Ministry for Education and Research (BMBF) under contract no. 05H21WWCAA and the German Research Foundation (DFG) under reference number DE 623/8-1. The authors acknowledge support from the COMETA COST Action CA22130.

## References

- [1] D. Buarque Franzosi et al., *Vector boson scattering processes: Status and prospects*, *Rev. Phys.* **8** (2022) 100071, [[arXiv:2106.01393](#)].
- [2] R. Covarelli, M. Pellen, and M. Zaro, *Vector-Boson scattering at the LHC: Unraveling the electroweak sector*, *Int. J. Mod. Phys. A* **36** (2021) 2130009, [[arXiv:2102.10991](#)].
- [3] **ATLAS** Collaboration, M. Aaboud et al., *Measurement of the production cross section of three isolated photons in  $pp$  collisions at  $\sqrt{s} = 8$  TeV using the ATLAS detector*, *Phys. Lett. B* **781** (2018) 55–76, [[arXiv:1712.07291](#)].

- [4] **ATLAS** Collaboration, G. Aad et al., *Evidence of  $W\gamma\gamma$  Production in  $pp$  Collisions at  $\sqrt{s} = 8$  TeV and Limits on Anomalous Quartic Gauge Couplings with the ATLAS Detector*, *Phys. Rev. Lett.* **115** (2015) 031802, [[arXiv:1503.03243](#)].
- [5] **CMS** Collaboration, A. M. Sirunyan et al., *Measurements of the  $pp \rightarrow W\gamma\gamma$  and  $pp \rightarrow Z\gamma\gamma$  cross sections and limits on anomalous quartic gauge couplings at  $\sqrt{s} = 8$  TeV*, *JHEP* **10** (2017) 072, [[arXiv:1704.00366](#)].
- [6] **ATLAS** Collaboration, G. Aad et al., *Measurements of  $Z\gamma$  and  $Z\gamma\gamma$  production in  $pp$  collisions at  $\sqrt{s} = 8$  TeV with the ATLAS detector*, *Phys. Rev. D* **93** (2016) 112002, [[arXiv:1604.05232](#)].
- [7] **CMS** Collaboration, S. Chatrchyan et al., *Search for  $WW\gamma$  and  $WZ\gamma$  production and constraints on anomalous quartic gauge couplings in  $pp$  collisions at  $\sqrt{s} = 8$  TeV*, *Phys. Rev. D* **90** (2014) 032008, [[arXiv:1404.4619](#)].
- [8] **ATLAS** Collaboration, M. Aaboud et al., *Study of  $WW\gamma$  and  $WZ\gamma$  production in  $pp$  collisions at  $\sqrt{s} = 8$  TeV and search for anomalous quartic gauge couplings with the ATLAS experiment*, *Eur. Phys. J. C* **77** (2017) 646, [[arXiv:1707.05597](#)].
- [9] **ATLAS** Collaboration, M. Aaboud et al., *Search for triboson  $W^\pm W^\pm W^\mp$  production in  $pp$  collisions at  $\sqrt{s} = 8$  TeV with the ATLAS detector*, *Eur. Phys. J. C* **77** (2017) 141, [[arXiv:1610.05088](#)].
- [10] **CMS** Collaboration, A. M. Sirunyan et al., *Search for the production of  $W^\pm W^\pm W^\mp$  events at  $\sqrt{s} = 13$  TeV*, *Phys. Rev. D* **100** (2019) 012004, [[arXiv:1905.04246](#)].
- [11] **ATLAS** Collaboration, G. Aad et al., *Evidence for the production of three massive vector bosons with the ATLAS detector*, *Phys. Lett. B* **798** (2019) 134913, [[arXiv:1903.10415](#)].
- [12] **ATLAS** Collaboration, G. Aad et al., *Observation of  $WWW$  Production in  $pp$  Collisions at  $\sqrt{s} = 13$  TeV with the ATLAS Detector*, *Phys. Rev. Lett.* **129** (2022) 061803, [[arXiv:2201.13045](#)].
- [13] **CMS** Collaboration, A. M. Sirunyan et al., *Observation of the Production of Three Massive Gauge Bosons at  $\sqrt{s} = 13$  TeV*, *Phys. Rev. Lett.* **125** (2020) 151802, [[arXiv:2006.11191](#)].
- [14] **ATLAS** Collaboration, *Prospect studies for the production of three massive vector bosons with the ATLAS detector at the High-Luminosity LHC*, .
- [15] B. Biedermann, A. Denner, and M. Pellen, *Large electroweak corrections to vector-boson scattering at the Large Hadron Collider*, *Phys. Rev. Lett.* **118** (2017) 261801, [[arXiv:1611.02951](#)].
- [16] A. Denner, S. Dittmaier, P. Maierhöfer, M. Pellen, and C. Schwan, *QCD and electroweak corrections to  $WZ$  scattering at the LHC*, *JHEP* **06** (2019) 067, [[arXiv:1904.00882](#)].
- [17] A. Denner, R. Franken, M. Pellen, and T. Schmidt, *NLO QCD and EW corrections to vector-boson scattering into  $ZZ$  at the LHC*, *JHEP* **11** (2020) 110, [[arXiv:2009.00411](#)].
- [18] A. Denner, R. Franken, T. Schmidt, and C. Schwan, *NLO QCD and EW corrections to vector-boson scattering into  $W^+ W^-$  at the LHC*, *JHEP* **06** (2022) 098, [[arXiv:2202.10844](#)].
- [19] B. Biedermann, A. Denner, and M. Pellen, *Complete NLO corrections to  $W^+ W^+$  scattering and its irreducible background at the LHC*, *JHEP* **10** (2017) 124, [[arXiv:1708.00268](#)].
- [20] A. Denner, R. Franken, M. Pellen, and T. Schmidt, *Full NLO predictions for vector-boson*



- scattering into  $Z$  bosons and its irreducible background at the LHC, *JHEP* **10** (2021) 228, [[arXiv:2107.10688](#)].
- [21] M. Chiesa, A. Denner, J.-N. Lang, and M. Pellen, *An event generator for same-sign  $W$ -boson scattering at the LHC including electroweak corrections*, *Eur. Phys. J. C* **79** (2019) 788, [[arXiv:1906.01863](#)].
- [22] A. Ballestrero, G. Bevilacqua, and E. Maina, *A complete parton level analysis of boson-boson scattering and electroweak symmetry breaking in  $\ell\nu + \text{four jets}$  production at the LHC*, *JHEP* **05** (2009) 015, [[arXiv:0812.5084](#)].
- [23] A. Denner, D. Lombardi, and C. Schwan, *Double-pole approximation for leading-order semi-leptonic vector-boson scattering at the LHC*, [[arXiv:2406.12301](#)].
- [24] A. Lazopoulos, K. Melnikov, and F. Petriello, *QCD corrections to tri-boson production*, *Phys. Rev. D* **76** (2007) 014001, [[hep-ph/0703273](#)].
- [25] T. Binoth, G. Ossola, C. G. Papadopoulos, and R. Pittau, *NLO QCD corrections to tri-boson production*, *JHEP* **06** (2008) 082, [[arXiv:0804.0350](#)].
- [26] D. T. Nhung, L. D. Ninh, and M. M. Weber, *NLO corrections to  $WWZ$  production at the LHC*, *JHEP* **12** (2013) 096, [[arXiv:1307.7403](#)].
- [27] S. Dittmaier, A. Huss, and G. Knippen, *Next-to-leading-order QCD and electroweak corrections to  $WWW$  production at proton-proton colliders*, *JHEP* **09** (2017) 034, [[arXiv:1705.03722](#)].
- [28] Y.-B. Shen, et al., *NLO QCD + NLO EW corrections to  $WZZ$  productions with leptonic decays at the LHC*, *JHEP* **10** (2015) 186, [[arXiv:1507.03693](#)]. [Erratum: *JHEP* **10**, 156 (2016)].
- [29] Y.-B. Shen, R.-Y. Zhang, W.-G. Ma, X.-Z. Li, and L. Guo, *NLO QCD and electroweak corrections to  $WWW$  production at the LHC*, *Phys. Rev. D* **95** (2017) 073005, [[arXiv:1605.00554](#)].
- [30] V. Hankele and D. Zeppenfeld, *QCD corrections to hadronic  $WWZ$  production with leptonic decays*, *Phys. Lett. B* **661** (2008) 103–108, [[arXiv:0712.3544](#)].
- [31] F. Campanario, V. Hankele, C. Oleari, S. Prestel, and D. Zeppenfeld, *QCD corrections to charged triple vector boson production with leptonic decay*, *Phys. Rev. D* **78** (2008) 094012, [[arXiv:0809.0790](#)].
- [32] M. Schönherr, *Next-to-leading order electroweak corrections to off-shell  $WWW$  production at the LHC*, *JHEP* **07** (2018) 076, [[arXiv:1806.00307](#)].
- [33] S. Dittmaier, G. Knippen, and C. Schwan, *Next-to-leading-order QCD and electroweak corrections to triple- $W$  production with leptonic decays at the LHC*, *JHEP* **02** (2020) 003, [[arXiv:1912.04117](#)].
- [34] A. Denner, M. Pellen, M. Schönherr, and S. Schumann, *Tri-boson and  $WH$  production in the  $W^+W^+jj$  channel: predictions at full NLO accuracy and beyond*, [[arXiv:2406.11516](#)].
- [35] **Sherpa** Collaboration, E. Bothmann et al., *Event Generation with Sherpa 2.2*, *SciPost Phys.* **7** (2019) 034, [[arXiv:1905.09127](#)].
- [36] S. Kallweit, J. M. Lindert, P. Maierhöfer, S. Pozzorini, and M. Schönherr, *NLO QCD+EW predictions for  $V + \text{jets}$  including off-shell vector-boson decays and multijet merging*, *JHEP* **04** (2016) 021, [[arXiv:1511.08692](#)].

- [37] C. Gütschow, J. M. Lindert, and M. Schönherr, *Multi-jet merged top-pair production including electroweak corrections*, *Eur. Phys. J. C* **78** (2018) 317, [[arXiv:1803.00950](#)].
- [38] R. Bellan, et al., *A sensitivity study of triboson production processes to dimension-6 EFT operators at the LHC*, *JHEP* **08** (2023) 158, [[arXiv:2303.18215](#)].
- [39] E. Celada, G. Durieux, K. Mimasu, and E. Vryonidou, *Triboson production in the SMEFT*, [[arXiv:2407.09600](#)].
- [40] S. Actis, A. Denner, L. Hofer, A. Scharf, and S. Uccirati, *Recursive generation of one-loop amplitudes in the Standard Model*, *JHEP* **04** (2013) 037, [[arXiv:1211.6316](#)].
- [41] S. Actis, et al., *RECOLA: REcursive Computation of One-Loop Amplitudes*, *Comput. Phys. Commun.* **214** (2017) 140–173, [[arXiv:1605.01090](#)].
- [42] A. Denner, S. Dittmaier, and L. Hofer, *COLLIER: a fortran-based Complex One-Loop Library in Extended Regularizations*, *Comput. Phys. Commun.* **212** (2017) 220–238, [[arXiv:1604.06792](#)].
- [43] A. Denner and S. Dittmaier, *Reduction of one-loop tensor 5-point integrals*, *Nucl. Phys. B* **658** (2003) 175–202, [[hep-ph/0212259](#)].
- [44] A. Denner and S. Dittmaier, *Reduction schemes for one-loop tensor integrals*, *Nucl. Phys. B* **734** (2006) 62–115, [[hep-ph/0509141](#)].
- [45] A. Denner and S. Dittmaier, *Scalar one-loop 4-point integrals*, *Nucl. Phys. B* **844** (2011) 199–242, [[arXiv:1005.2076](#)].
- [46] A. Denner, G. Pelliccioli, and C. Schwan, *NLO QCD and EW corrections to off-shell  $t\bar{z}$  production at the LHC*, *JHEP* **10** (2022) 125, [[arXiv:2207.11264](#)].
- [47] S. Catani and M. Seymour, *A general algorithm for calculating jet cross-sections in NLO QCD*, *Nucl. Phys. B* **485** (1997) 291–419, [[hep-ph/9605323](#)]. [Erratum: *Nucl. Phys. B* **510** (1998) 503–504].
- [48] S. Dittmaier, *A general approach to photon radiation off fermions*, *Nucl. Phys. B* **565** (2000) 69–122, [[hep-ph/9904440](#)].
- [49] S. Catani, S. Dittmaier, M. H. Seymour, and Z. Trocsanyi, *The dipole formalism for next-to-leading order QCD calculations with massive partons*, *Nucl. Phys. B* **627** (2002) 189–265, [[hep-ph/0201036](#)].
- [50] S. Dittmaier, A. Kabelschacht, and T. Kasprzik, *Polarized QED splittings of massive fermions and dipole subtraction for non-collinear-safe observables*, *Nucl. Phys. B* **800** (2008) 146–189, [[arXiv:0802.1405](#)].
- [51] A. Denner, S. Dittmaier, M. Roth, and D. Wackerroth, *Predictions for all processes  $e^+e^- \rightarrow 4$  fermions +  $\gamma$* , *Nucl. Phys.* **B560** (1999) 33–65, [[hep-ph/9904472](#)].
- [52] A. Denner, S. Dittmaier, M. Roth, and L. H. Wieders, *Electroweak corrections to charged-current  $e^+e^- \rightarrow 4$  fermion processes: Technical details and further results*, *Nucl. Phys.* **B724** (2005) 247–294, [[hep-ph/0505042](#)]. [Erratum: *Nucl. Phys. B* **854** (2012) 504].
- [53] A. Denner and S. Dittmaier, *The complex-mass scheme for perturbative calculations with unstable particles*, *Nucl. Phys. B Proc. Suppl.* **160** (2006) 22–26, [[hep-ph/0605312](#)].
- [54] A. Denner and S. Dittmaier, *Electroweak Radiative Corrections for Collider Physics*, *Phys. Rept.* **864** (2020) 1–163, [[arXiv:1912.06823](#)].
- [55] T. Kinoshita, *Mass singularities of Feynman amplitudes*, *J. Math. Phys.* **3** (1962) 650–677.

- [56] T. D. Lee and M. Nauenberg, *Degenerate systems and mass singularities*, *Phys. Rev.* **133** (Mar, 1964) B1549–B1562.
- [57] A. Denner, S. Dittmaier, M. Pellen, and C. Schwan, *Low-virtuality photon transitions  $\gamma^* \rightarrow f\bar{f}$  and the photon-to-jet conversion function*, *Phys. Lett. B* **798** (2019) 134951, [[arXiv:1907.02366](#)].
- [58] A. Denner, L. Hofer, A. Scharf, and S. Uccirati, *Electroweak corrections to lepton pair production in association with two hard jets at the LHC*, *JHEP* **01** (2015) 094, [[arXiv:1411.0916](#)].
- [59] A. Denner, S. Dittmaier, T. Gehrmann, and C. Kurz, *Electroweak corrections to hadronic event shapes and jet production in  $e^+e^-$  annihilation*, *Nucl. Phys. B* **836** (2010) 37–90, [[arXiv:1003.0986](#)].
- [60] A. Denner, S. Dittmaier, T. Kasprzik, and A. Mück, *Electroweak corrections to  $W + jet$  hadroproduction including leptonic  $W$ -boson decays*, *JHEP* **08** (2009) 075, [[arXiv:0906.1656](#)].
- [61] E. W. N. Glover and A. G. Morgan, *Measuring the photon fragmentation function at LEP*, *Z. Phys. C* **62** (1994) 311–322.
- [62] **ALEPH** Collaboration, D. Buskulic et al., *First measurement of the quark to photon fragmentation function*, *Z. Phys. C* **69** (1996) 365–378.
- [63] **Particle Data Group** Collaboration, R. L. Workman et al., *Review of Particle Physics*, *PTEP* **2022** (2022) 083C01.
- [64] D. Yu. Bardin, A. Leike, T. Riemann, and M. Sachwitz, *Energy-dependent width effects in  $e^+e^-$  annihilation near the  $Z$ -boson pole*, *Phys. Lett.* **B206** (1988) 539–542.
- [65] A. Denner, S. Dittmaier, M. Roth, and D. Wackerroth, *Electroweak radiative corrections to  $e^+e^- \rightarrow WW \rightarrow 4$  fermions in double pole approximation: The RACOONWW approach*, *Nucl. Phys.* **B587** (2000) 67–117, [[hep-ph/0006307](#)].
- [66] S. Dittmaier and M. Krämer, *Electroweak radiative corrections to  $W$  boson production at hadron colliders*, *Phys. Rev. D* **65** (2002) 073007, [[hep-ph/0109062](#)].
- [67] **NNPDF** Collaboration, R. D. Ball et al., *Photons in the proton: implications for the LHC*, *Eur. Phys. J. C* **84** (2024) 540, [[arXiv:2401.08749](#)].
- [68] A. Buckley, et al., *LHAPDF6: parton density access in the LHC precision era*, *Eur. Phys. J. C* **75** (2015) 132, [[arXiv:1412.7420](#)].
- [69] M. Cacciari, G. P. Salam, and G. Soyez, *The anti- $k_t$  jet clustering algorithm*, *JHEP* **04** (2008) 063, [[arXiv:0802.1189](#)].
- [70] A. Ballestrero et al., *Precise predictions for same-sign  $W$ -boson scattering at the LHC*, *Eur. Phys. J. C* **78** (2018) 671, [[arXiv:1803.07943](#)].